

The 2016 January eruption of recurrent Nova LMC 1968

N. P. M. Kuin ¹, ¹★ K. L. Page ², P. Mróz, ³ M. J. Darnley ⁴, S. N. Shore, ^{5,6}
 J. P. Osborne ², F. Walter, ⁷ F. Di Mille, ⁸ N. Morrell, ⁸ U. Munari, ⁹ T. Bohlsen, ¹⁰
 A. Evans, ¹¹ R. D. Gehrz, ¹² S. Starrfield, ¹³ M. Henze, ^{14,15} S. C. Williams ¹⁶,
 G. J. Schwarz, ¹⁷ A. Udalski, ³ M. K. Szymański ³, R. Poleski, ^{3,18} I. Soszyński, ³
 V. A. R. M. Ribeiro, ^{19,20} R. Angeloni, ^{21,22} A. A. Breeveld, ¹ A. P. Beardmore ² and
 J. Skowron ³

Affiliations are listed at the end of the paper

Accepted 2019 October 18. Received 2019 October 17; in original form 2019 September 10

ABSTRACT

We present a comprehensive review of all observations of the eclipsing recurrent Nova LMC 1968 in the Large Magellanic Cloud which was previously observed in eruption in 1968, 1990, 2002, 2010, and most recently in 2016. We derive a probable recurrence time of 6.2 ± 1.2 yr and provide the ephemerides of the eclipse. In the ultraviolet–optical–IR photometry the light curve shows high variability right from the first observation around 2 d after eruption. Therefore no colour changes can be substantiated. Outburst spectra from 2016 and 1990 are very similar and are dominated by H and He lines longward of 2000 Å. Interstellar reddening is found to be $E(B - V) = 0.07 \pm 0.01$. The super soft X-ray luminosity is lower than the Eddington luminosity and the X-ray spectra suggest the mass of the white dwarf (WD) is larger than $1.3 M_{\odot}$. Eclipses in the light curve suggest that the system is at high orbital inclination. On day 4 after the eruption a recombination wave was observed in Fe II ultraviolet absorption lines. Narrow-line components are seen after day 6 and explained as being due to reionization of ejecta from a previous eruption. The UV spectrum varies with orbital phase, in particular a component of the He II 1640 Å emission line, which leads us to propose that early-on the inner WD Roche lobe might be filled with a bound opaque medium prior to the re-formation of an accretion disc. Both this medium and the ejecta can cause the delay in the appearance of the soft X-ray source.

Key words: binaries: eclipsing – stars: individual: (Nova LMC 1968) – novae, cataclysmic variables – ultraviolet: stars – X-rays: binaries.

1 INTRODUCTION

Nova eruptions are the result of the high-speed ejection of a turbulent mass (Casanova et al. 2016; Figueira et al. 2018) due to a thermonuclear runaway (TNR) occurring within the surface layer of a mass-accreting white dwarf (WD; see Bode & Evans 2008; Woudt & Ribeiro 2014; Starrfield, Iliadis & Hix 2016, for recent review articles). Osborne (2015) provides a recent review of X-ray observations of novae. In these close, semi-detached, binary systems the non-degenerate low-mass donor can be a main-sequence star, a sub-giant, or a red giant (see Darnley et al. 2012, for a summary). Novae that have been observed in eruption just once – the majority of systems – make up the group of classical

novae, of which there are around 2000 known systems across the Milky Way and nearby galaxies. All novae are predicted to repeat (Priyalnik & Kovetz 1995; Yaron et al. 2005), and a small subset, the recurrent novae (RNe) have been observed in eruption more than once. Observed recurrence periods range from $P_{\text{rec}} \simeq 1$ yr (for M31N 2008-12a; Darnley et al. 2014) up to 98 yr (V2487 Ophiuchi; Pagnotta et al. 2009) – although the upper end must be a selection effect.

The short inter-eruption time-scales of the RNe are believed to be due to a combination of a high-mass WD and a high-mass accretion rate (Starrfield, Sparks & Shaviv 1988b); the RNe contain many of the highest mass WDs known. Within the Milky Way there are 10 confirmed RNe, including the sub-class prototypes RS Ophiuchi ($P_{\text{rec}} \simeq 20$ yr; with a red giant donor; see Evans et al. 2008, for detailed reviews) and U Scorpii (mean $P_{\text{rec}} = 10.3$ yr; sub-giant donor; see, e.g. Pagnotta et al. 2015, and references therein).

* E-mail: n.kuin@ucl.ac.uk

Schaefer (2010) provided a detailed review of the known Galactic RNe; this and similar work indicated that the required high-mass accretion rate is in most cases provided by mass-loss from an evolved donor (sub- or red giant). Pagnotta & Schaefer (2014) went on to estimate that the true RN population ($10 \text{ yr} \leq P_{\text{rec}} \leq 100 \text{ yr}$; A. Pagnotta, private communication) of the Milky Way may be as high as 25 ± 10 per cent of all Galactic novae. In recent years some very rapid recurrent novae (RRNe) have been found with mean $P_{\text{rec}} < 10 \text{ yr}$. The best studied is M31N 2008-12a that has been detected in eruption every year since 2008 (see Darnley et al. 2014, 2015, 2016a; Henze et al. 2014b, 2015, 2018; Tang et al. 2014), with a mean $P_{\text{rec}} = 0.99 \pm 0.02 \text{ yr}$ (Darnley & Henze 2019), which is surrounded by the super-remnant of thousands of earlier eruptions (Darnley et al. 2019). Theoretical studies of RRNe point to the presence very high-mass WDs with high-mass accretion rates and low ejected mass (e.g. Starrfield et al. 1988b; Prialnik & Kovetz 1995; Yaron et al. 2005; Wolf et al. 2013). Therefore, in RRNe the ejecta become transparent on a much shorter time-scale (than their CN counterparts), which opens the opportunity to study the evolution of the underlying system just after the eruption.

Extragalactic systems with their known distance often prove more suitable environments for the study of nova populations, and our near neighbour M31 is by far the best-studied example (see Darnley & Henze 2018, for a recent review). M31 has an observed nova rate of $65_{-15}^{+16} \text{ yr}^{-1}$ (Darnley et al. 2006) and over 1100 suspected novae have been discovered in that host alone (see Pietsch et al. 2007; Pietsch 2010, and their on-line database¹). Shafter et al. (2015) compiled a catalogue of 16 M31 RNe and indicated that up to a third of M31 nova eruptions may be due to RNe ($P_{\text{rec}} \leq 100 \text{ yr}$). Using an independent approach, Williams et al. (2016) indicated that 30_{-10}^{+13} per cent of M31 novae harboured red giant donors – with an implication of a high-mass accretion rate – and that these systems were strongly associated with the disc of M31. Although Nova LMC 1968 (N LMC 1968), the subject of this paper, was the first *confirmed* extragalactic nova (see Section 2), Shafter et al. (2015) reported that the M31 nova M31N 1926-06a (Hubble 1929) was the first extragalactic nova to be observed to recur (as M31N 1962-11a; see Rosino 1964; Börngen 1968; Henze, Meusinger & Pietsch 2008).

The first nova in the Large Magellanic Cloud (LMC; LMCN 1926-09a) was reported by Luyten (1927). Since then there have been 50 unique LMC nova candidates (see Shafter 2013, and on-line catalogue¹), around half of which have been spectroscopically confirmed. Mróz et al. (2016) recently computed the global nova rate of the LMC to be $2.4 \pm 0.8 \text{ yr}^{-1}$. Within the LMC there are four known RNe, YY Doradus (LMCN 1937; Bond et al. 2004; Mason et al. 2004b), LMCN 1971-08a (Bode et al. 2016), OGLE-2018-NOVA-01 (LMCN 2018-02a; Mroz & Udalski 2018), and Nova LMC 1968 (Shore et al. 1991). Shafter (2013) concluded that ~ 10 per cent of LMC novae are recurrent, and that ~ 16 per cent of observed LMC eruptions occur from RN systems, though uncertainties are large since these numbers are based on four RNe only. For comparison, 22 nova candidates have been discovered in the Small Magellanic Cloud¹ which with its known distance provides good multispectral coverage opportunities (Aydi et al. 2018). Mróz et al. (2016) compute a nova rate of $0.9 \pm 0.4 \text{ yr}^{-1}$. There are no known RNe in the SMC.

The geometry of novae ejecta is non-spherical. Axially symmetric geometries were first discussed by Gaposchkin (1957). Morpho-

kinematical emission-line profile modelling with SHAPE² (Ribeiro et al. 2013a; Ribeiro, Munari & Valisa 2013b) shows bipolar geometries. Recent Monte Carlo based radiative transfer models of ejecta far enough after the eruption to ensure low densities and frozen-in state provide good fits to cone-shape geometries (Shore et al. 2013a,b, 2016) and can include embedded dust (Shore et al. 2018).

If a carbon–oxygen (CO) WD approaches and passes the Chandrasekhar (1931) mass a type Ia supernovae (SN Ia) thermonuclear explosion may ensue (see e.g. Whelan & Iben 1973; Hillebrandt & Niemeyer 2000; Livio & Mazzali 2018), whereas accreting oxygen–neon WDs are predicted to collapse to neutron stars (see e.g. Gutierrez et al. 1996). Novae have long been a proposed SN Ia progenitor pathway; the two difficulties have been the unknown composition of the massive WDs found in RNe, and the relatively low number of systems. However, recent work by Hillman et al. (2016) has indicated that an accreting CO WD can grow from its formation mass ($< 1.1 M_{\odot}$) up to the Chandrasekhar mass with little or no tuning of the system parameters (see also Hernanz & José 2008; Starrfield et al. 2012), whereas work by Pagnotta & Schaefer (2014), Shafter et al. (2015), and Williams et al. (2016) has indicated that the underlying size of the RN population may be larger than first determined, as may be the global nova rates themselves (also see Chen et al. 2016; Shara et al. 2016; Soraisam et al. 2016; Shafter 2017).

In this paper we present panchromatic observations, from the near-infrared to the X-ray, of the 2016 January eruption of the rapidly recurring N LMC 1968. We also revisit observations from previous eruptions. In Section 2 we provide a summary of the eruption history of the system. In Section 3 we present the observations, give the orbital ephemerides, the light curve and X-ray data analyses. In Section 4 the WD mass, reddening, secondary star, the discovery of a recombination wave in Fe^+ , and narrow-line profiles are discussed. In Section 5 an estimate of the mass ejected, He mass addition from H burned during the SSS phase, orbital inclination, and accretion disc formation are discussed in the context of a comprehensive model. Section 6 provides a brief summary of some of the main points and a table summarizing the derived parameters.

2 THE RECURRENT NOVA LMC 1968

N LMC 1968 (originally referred to as Nova Mensae 1968; Sievers 1970) was first discovered in eruption at a magnitude of $m_{\text{pg}} = 10.9$ on Bamberg plates taken by I. Paterson on 1968 December 16.5 UT. By virtue of its decline rate of 0.5 mag d^{-1} (see Section 3.3), the speed class (see Gaposchkin 1957) of this eruption was classified as ‘fast’. The best estimate for the onset of the 1968 eruption is $\text{MJD } 40206 \pm 1$ (Sievers 1970). Subsequently, this nova has been seen in eruption a further four times, most recently in 2016 January. The 1990, 2002, and 2010 eruptions are summarized below, and the 2016 eruption is introduced.

2.1 Nova LMC 1990b

On 1990 February 14.1 UT (MJD 47936.1) Nova LMC 1990b was discovered in eruption at $m_{\text{pv}} = 11.2 \text{ mag}$, close to the position of N LMC 1968 (Liller 1990), see Fig. 1 for a recent finder chart. A direct comparison of the Nova LMC 1990b position to that of N

¹<http://www.mpe.mpg.de/m31novae/opt/>

²<http://bufadora.astrosen.unam.mx/shape/index.html>

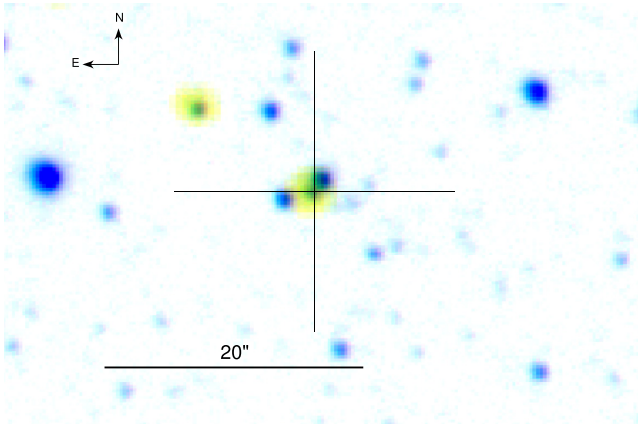


Figure 1. The finding chart of the nova. North is up and East is to the left. RGB inverted composite of UVOT *uvm2* (yellow), OGLE *I* band (magenta), *V* band (cyan). The black cross marks the nova position.

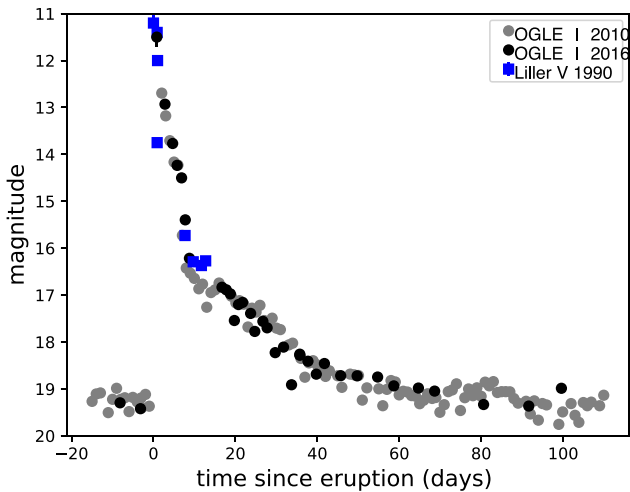


Figure 2. A comparison between the OGLE *I*-band data from the 2010 and 2016 eruptions of N LMC 1968. The *V*-band photometry from Liller et al. (2004) of the 1990 eruption is included as blue squares.

LMC 1968 using the original photographic plates showed a match in R.A. within 2.4 arcsec and in December within 6 arcsec (Shore et al. 1991). The peak time of eruption is more difficult to establish, as the last pre-eruption observation was on 1990 February 3 (Liller, Shida & Jones 2004), 11 d pre-discovery. However, the photometry matches that of later eruptions well (see Fig. 2) and based on that the discovery time would be within 0.2 d of the eruption.

Optical spectra of the 1990 eruption were obtained by Shara and Moffat (Williams et al. 2003) providing confirmation of the nova, thereby identifying Nova LMC 1990b as the first *spectroscopically confirmed* extragalactic RN and on day 9 by Williams et al. (2003) at the Cerro Tololo Inter-American Observatory (CTIO) in Chile. Sekiguchi et al. (1990) obtained photometry and spectra on day 8.7, 9.7, 11.7, and 15.7 at the SAAO in Sutherland, South Africa. Judging by the comparison of the 1990 mag at discovery to the well-observed 2010 and 2016 light curves, the (now lost) discovery spectrum was likely obtained within a day post-eruption though no time was reported in the IAU Circular 4964 of 15 February 1990. The discovery spectrum showed He I and He II 4686 Å lines

with expansion velocities of 5500 km s^{-1} , and broad double-peaked Balmer lines (Williams et al. 2003), which ‘one tends not to see that shortly after eruption’ (Williams, private communication). The 1990 eruption was deemed to be spectrally similar to the Galactic recurrent nova U Sco, with a similarly fast evolution.

Nova LMC 1990b was well observed with the International Ultraviolet Explorer (*IUE*) satellite which covered the eruption in the 1050–3250 Å wavelength range starting just 2 d after the discovery of the 1990 eruption, and observing on days 3, 5, 9, 14, 32, and 38 (Shore et al. 1991). The He/H ratio derived from the *IUE* spectra by Shore et al. (1991) was exceptionally high and seen as evidence for an evolved companion. The total UV luminosity was shown by Shore et al. (1991) to be large, possibly exceeding the Eddington luminosity for a Solar mass WD. Shore et al. (1991) used a value of $E(B - V) = 0.15 \text{ mag}$ and the Fitzpatrick extinction curve (Fitzpatrick 1986) and thus applied an extinction correction larger than we currently believe is correct (see Section 4.3). Since 1990, the LMC distance has also been revised downward from 55 to $49.59 \pm 0.60 \text{ kpc}$ (Pietrzyński et al. 2013; Bhardwaj et al. 2017; Pietrzyński et al. 2019), which is the distance we adopt in this paper. We revisit below the question of the luminosity in light of the reduced extinction and distance. Shore et al. (1991) derived an accretion rate $M_{\text{acc}} \geq 10^{-8.6 \pm 0.5} M_{\odot} \text{ yr}^{-1}$ based on an estimated mass ejection of $M_{\text{ej}} = 10^{-7.3 \pm 0.5} M_{\odot}$ which may have been overestimated; the mean velocity width of the UV lines (FWZI) was 12000 km s^{-1} with a full width at half-maximum (FWHM) of 5000 km s^{-1} . The paucity of optical spectra of the 1990 eruption left open the question of whether the UV-optical derived He/H ratio was probing the same region of ejecta as the optical observations.

2.2 Missed eruptions?

The nova was almost continuously observed by the MACHO microlensing survey (Alcock et al. 1992, 2000) during the years 1993–1999 and there is no evidence for further eruptions in the available data. Eruptions of N LMC 1968 last ~ 50 d; however the initial decline essentially takes 15 d. There are a few gaps in the MACHO data as long as 40–60 d and there is thus a small probability that the nova erupted during these gaps. The limit for the MACHO observations in the LMC is $V \approx 18$ (the LMC sky background is $R \approx 19.5 \text{ mag arcsec}^{-2}$; Alcock et al. 1999), so an eruption would be detected significantly for up to 40 d, see Fig. 2. Based on the MACHO coverage of the LMC and assuming the nova can no longer be observed 40 d after eruption, the probability for a missed eruption is just 4 per cent.

2.3 The 2002 eruption

In 2002 the All Sky Automated Survey (ASAS-3) observed the nova region on every other day (Pojmanski 2002). On 2002 October 9, 7:18 UT (MJD 52556.304) the nova was not seen, but there were positive detections of the 2002 eruption in two subsequent observations on 2002 October 11, 6:08 UT with $V = 11.15 \pm 0.02$ and with $V = 14.17 \pm 0.13$ on 2002 October 15, 5:20 UT. The 2002 eruption was also observed by the Expérience pour la Recherche d’Objets Sombres (EROS) group (Tisserand & Marquette, private communication; Tisserand et al. 2007). Unfortunately, a useful light curve could not be extracted from the EROS data. Based on the above we conclude that the 2002 eruption peaked between MJD 52556.3 and 52558.3 (i.e. 2002 October 10).

Table 1. Known eruptions of N LMC 1968.

Discovery date	Positions ^a RA, Dec. (J2000)		Adopted eruption dates (MJD)	Discovery magnitude ^b
1968 Dec. 16.5	05:10:00[06]	−71:39:05[60]	40206.0 ± 1.5	$m_{\text{pg}} = 10.9$
1990 Feb. 14.1	05:09:58.3[.5]	−71:39:51.3[6]	47936.1 ± ?	$m_{\text{pv}} = 11.2$
2002 Oct. 10	05:09:59.4	−71:39:51.5	52557.3 ± 1.0	$V = 11.15 \pm 0.02$
2010 Nov. 21.2	05:09:58.39[.01]	−71:39:52.7[.1]	55521.2 ± 1.0	$I = 11.7 \pm 0.3$
2016 Jan. 21.2	05:09:58.39[.01]	−71:39:52.7[.1]	57407.4 ± 0.8	$I \approx 11.5 \pm 0.2$

^aPositional uncertainties are given in square brackets.^bThe discovery magnitude is not necessarily the peak magnitude.

2.4 Nova LMC 2010

The next detected eruption of N LMC 1968 occurred on 2010 November 21.2 UT (MJD 55521.2 ± 1.0) with a peak observed magnitude 11.7 ± 0.3 (Mróz et al. 2014) and was discovered by the Optical Gravitational Lensing Experiment (OGLE; see Udalski et al. 2008; Udalski, Szymański & Szymański 2015). The coordinates of the nova were measured to be $\alpha = 5^{\text{h}}9^{\text{m}}58^{\text{s}}.39$, $\delta = -71^{\circ}39'52''.7$ (J2000) from the OGLE data, with an astrometric accuracy of 0".1. A detailed analysis is provided in Section 3.3.

2.5 Nova LMC 2016

The most recent eruption of N LMC 1968 was discovered by OGLE on 2016 January 21.2094 UT at a reported magnitude $I \leq 11.5$ (Mroz & Udalski 2016). The previous OGLE observation on January 17.2363 indicated that the nova was still at quiescence ($I \simeq 19$ mag). This eruption was assigned the internal OGLE designation OGLE-2016-NOVA-01.

The 2016 eruption must have peaked between January 19.65000 UT (which is the last non-detection from the AAVSO³ database) and January 21.20942 UT (the OGLE detection). The mean time is JD 2457 407.9 = January 20.4 ± 0.8 which we define as t_0 , the best estimate of the time of eruption, see Table 1. For the 2016 eruption on JD = 2457 408.709 we estimate the magnitude, near the peak, is $I = 11.5 \pm 0.2$ mag, close to those of previous eruptions.

2.6 A rapidly recurring nova

Given the continuing monitoring from ASAS, and OGLE, the last three detected eruptions, 2002, 2010, and 2016 were likely to be subsequent eruptions. However, it is possible that between 1968 and 1990 several eruptions were missed. Considering that we had inter-eruption intervals (going back in time) of 1887, 2963, 4621, and 7731 d, from the three most recent eruptions we get an estimate of 2425 ± 540 d. Using the first three intervals while accounting for a missed eruption in 1996 gives a mean period of 2356 d, which suggests either two or three missed eruptions between 1968 and 1990. If we assume there were two missed eruptions we get a best estimate for the interval between eruptions of $P_{\text{rec}} = 6.2 \pm 1.2$ yr (two standard deviations) with the possibly missed eruptions centred around 1976 February and 1982 October.

With $P_{\text{rec}} < 10$ yr, we can therefore consider N LMC 1968 as one of the most rapid recurrents, and comparable to the Galactic RN U Sco. With all the other extragalactic examples being in M31, N LMC 1968 is the closest RRN with accurate distance, and therefore should be studied in much greater detail.

3 MULTISPECTRAL OBSERVATIONS

3.1 *Swift* observations (UVOT and XRT)

Upon discovery of the N LMC 2016 a Neil Gehrels *Swift* Observatory (Gehrels et al. 2004) target of opportunity observation started on 2016 January 23 06:40 UT (day 2.88) with the X-ray Telescope (XRT; Burrows et al. 2005) and the Ultraviolet and Optical Telescope (UVOT; Mason et al. 2004a; Roming et al. 2005) obtaining photometric data in the UV filters and UV grism spectra. Regular *Swift* observations continued until April 16 (day 85.5). The final XRT detection was on March 17 (day 56.1), with the remaining 5.5 ks of exposure only providing an X-ray upper limit. Due to an observing constraint,⁴ there were no *Swift* data between day 14.1 and day 24.1. *Swift* observations were not continued beyond this point since by that time the XRT count rate was too low and the contamination of the photometry by nearby sources was thought to be too large. However, additional UVOT observations were obtained on day 215–320. The processing of the *Swift* data is discussed in relation to similar multispectral data in the following sections.

3.2 XRT data reduction, the soft-X-ray light curve and variability

The *Swift* XRT observations started with a 500 s observation in Photon Counting (PC) mode. The XRT-detected faint hard X-ray emission at day 4 (Darnley et al. 2016b). A significant increase in X-ray counts below 1 keV was detected on January 27, only 6 d after discovery. This indicated the emergence of the supersoft X-ray source (SSS) emission – a phase that had never been observed before for this nova.⁵

The XRT data were processed and analysed using the standard HEASOFT tools and most up-to-date calibration files. All the X-ray data were collected in PC mode, and grades 0–12 were analysed for both the light curves and spectra. No pile-up was evident at any time, so a circular region was used to extract the source counts, with the radius changing from 10 to 15 pixels (1 pixel ≡ 2.36 arcsec) depending on the brightness of the source.

Fig. 3 plots the soft (0.3–1.5 keV) and hard (1.5–10 keV) band light curves. There are very few counts above 1.5 keV, and this flux fades rapidly. The X-ray count rate was approximately constant from the day of first detection (day 2.9) until day 6.1; the soft emission then increased in brightness from day 7.2 until day

⁴There is an area near its orbital pole which is unobservable to *Swift*, due to the requirement that the spacecraft point more than 30° from the Earth limb, which subtends an angle of ~66° to the orbital altitude. This pole constraint can prevent observations of a given target for several days.

⁵We checked for pre-*Swift* observations of N LMC 1968 in other X-ray and EUV mission catalogues; it was not detected.

³<https://www.aavso.org>

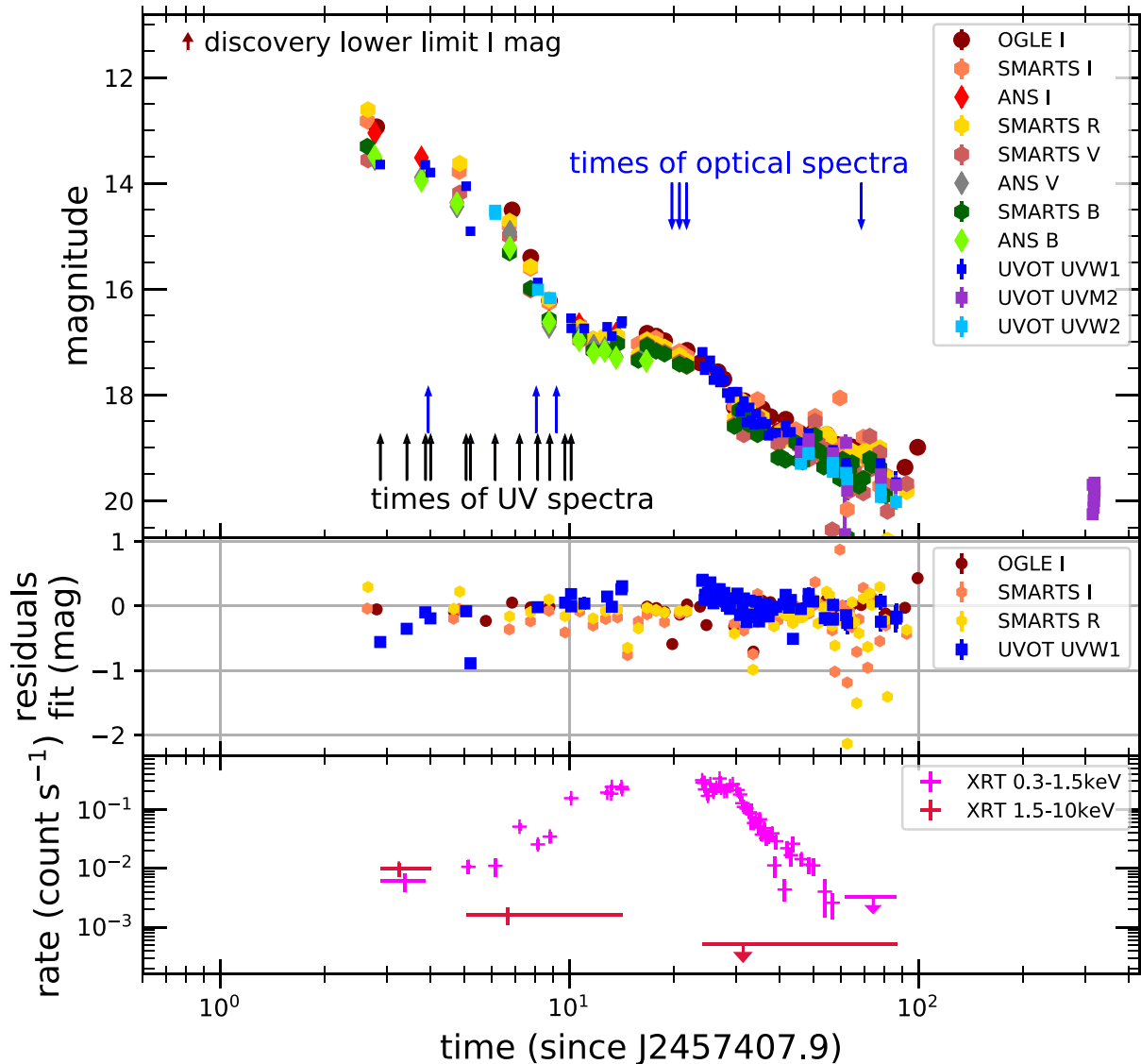


Figure 3. The optical, UV, and X-ray light curves for the 2016 eruption of Nova LMC 1968. Error bars are included, but in the UV/optical are mostly smaller than the symbols. The first *I* band was saturated, leading to a lower limit. In the top panel data which fell within 0.1 of orbital phase 0.0 were excluded. The middle panel shows the residuals for *I*, *R*, and *uvw1* from the light-curve fit, see Table 2; these include all observations. All panels have a common time axis where times are from the estimated eruption time. The times when spectra were obtained have been indicated. Note that the *BVRi* magnitudes are on the Vega system but the UV magnitudes are on the AB system. The X-ray light curves for the harder and softer photons have been separated to show the initial decline in hard photons and rise in soft emission.

14.1, reaching $\sim 0.25 \text{ count s}^{-1}$. At this point, the source became unobservable to *Swift*. The nova re-emerged from the observing constraint on day 24.1 at about the same count rate as 10 d previously and, after a short plateau phase, started to fade from day 31. The X-ray source was no longer detected after day 57, with a final 3σ upper limit $3.3 \times 10^{-3} \text{ count s}^{-1}$ (0.3–1.5 keV) using 5.5 ks of data collected between 62 and 87 d.

High-amplitude X-ray variability has been observed in several novae during the early SSS phase which is yet to be fully understood (see e.g. Ness et al. 2009; Osborne et al. 2011; Bode et al. 2016). These variations are seen to occur on time-scales from hours to days. Despite daily coverage during the first 12 d of the eruption, no large amplitude X-ray variability was seen during the rise of the SSS phase in N LMC 1968.

3.3 OGLE observations

N LMC 1968 has been monitored in the *V* and *I* bands as part of the ongoing OGLE survey since 2010. These observations were conducted using the 1.3 m Warsaw Telescope located at the Las Campanas Observatory, Chile. All data were reduced and calibrated following the standard OGLE pipeline (Udalski et al. 2015). Both the 2010 and 2016 eruptions were discovered by OGLE; the 2010 in archival data (Mróz et al. 2014; Mroz & Udalski 2016).

The nova has a close (≈ 1.2 arcsec distant) yet unrelated, bright, non-variable on-sky neighbour. Both stars are resolved in the OGLE photometry, see Fig. 1 which is a colour-coded composite image that also includes the UVOT *uvm2* band, which has a central wavelength of 2246 \AA (and has a broader point spread function than the ground-based data). OGLE uses differential image techniques, so the flux

is measured on the subtracted images and the effects of blending due to neighbouring stars is reduced.

Because both the 2010 and 2016 eruptions have been observed by OGLE, we can compare data taken by the same instrument for two subsequent eruptions. In Fig. 2 the *I*-band light curves of the 2010 and 2016 eruptions are shown for comparison, the similarity is clearly evident. Schaefer (2010) noted that all eruptions of a given RN appear essentially identical.

Using the estimated time of eruption, we find a decrease in the *I* band of two magnitudes after $t_2 = 3.9 \pm 0.8$ d, and three magnitudes after $t_3 = 5.9 \pm 0.8$ d, see Fig. 3.

3.4 SMARTS/Andicam photometry

BVR_{CI} photometry (Vega magnitudes) was obtained with the Andicam instrument on the Small and Moderate Aperture Research Telescope System (SMARTS) 1.3 m telescope at CTIO starting in February 2012, monitoring N LMC 1968 twice a year (Walter et al. 2012). Daily observations of the 2016 eruption were conducted from day 2 to 81 with a break between day 22 and 29, further observations on day 92 and 203 and continuing. No new eruption has been seen as of $t_0 + 1174$ d.

As noted before, there are two stars in close proximity to the nova on the sky. To separate these stars, we fit three two-dimensional Gaussians to each observation using the IDL routine MPFITFUN (Markwardt 2009)⁶ constrained to have the same widths. The distribution in flux between the three stars is given by the ratios of the best-fitting amplitudes. Since the data are noisy, and we do not a priori know the positions of the stars, we allow the centres of the Gaussians to wander within 1 pixel (0.37 arcsec) of the median position.

We determined the relative positions from the fits on 14 nights, January 29 through February 22, excluding nights with particularly bad seeing. The contribution of the nova to the summed flux dropped from 71 per cent to 24 per cent during this time. Relative to the nova, the mean offset positions are: SE star: $\Delta\alpha = -2.17 \pm 0.06$ arcsec, $\Delta\delta = -0.34 \pm 0.04$ arcsec; NW star: $\Delta\alpha = +0.88 \pm 0.07$ arcsec, $\Delta\delta = +1.08 \pm 0.08$ arcsec; see Fig. 1.

We calibrated the fluxes using aperture photometry in an 11 pixel (4.06 arcsec) aperture. We use 25 stars in the field as comparisons. They are calibrated against Landolt standard stars on photometric nights to determine their magnitudes.

3.5 ANS photometry

BVI_C optical photometry of the nova was obtained with the Asagio Novae and Symbiotic stars (ANS) collaboration (Munari et al. 2012) robotic telescope, described by Munari & Moretti (2012), located in San Pedro de Atacama (Chile). Detailed analysis of the photometric performances and multi-epoch measurements of the actual transmission profiles for the photometric filter sets in use is presented by Munari & Moretti (2012). Data reduction used the APASS sources for calibration (Henden et al. 2012; Munari & Valisa 2014) using the transformation equation calibrated in Munari et al. (2014a, 2014b). The APASS survey is strictly linked to the Landolt (2009) and Smith et al. (2002) systems of equatorial standards.

All measurements were carried out with aperture photometry, with the aperture radius and inner/outer radii for the sky annulus χ^2 -optimized on each image to reduce dispersion of the stars in the local

photometric sequences around the transformation equations from the local instantaneous to the standard system. Finally, colours and magnitudes were obtained separately during the reduction process, and were not derived one from the other. The quoted uncertainties include all error sources. Magnitudes are on the Vega system. The nearby stars contaminate the photometry due to the large ANS PSF so that the data fainter than 16th magnitude cannot be used without a correction. There are enough faint data points to be useful. To fit ANS to the OGLE and SMARTS photometry, the ANS magnitude was transformed using

$$\text{mag}_{\text{corr}} = 2.5 \times \log_{10} [10^{-0.4(V+a)} - b] \quad (1)$$

with $a_I = 0.7$, $b_I = 8 \times 10^4$, $a_V = 0.3$, $b_V = 3 \times 10^{-8}$, $a_B = 0.4$, and $b_B = 3 \times 10^4$.

Munari et al. (2016) report the early $BVRI$ photometry from SMARTS/Andicam and the Asagio Novae and ANS combined.

3.6 Swift UVOT photometry

Swift UVOT obtained UV photometry from day 2.88 until day 14, from day 24 to day 86, and from day 315 to day 320. The photometry was processed using the UVOT FT00L UVOTPRODUCT and the 20160321 version of the *Swift* CALDB. In addition a verification was made to eliminate observations that fell on areas of reduced sensitivity using the provisional small-scale sensitivity map for UVOT.⁷ The *Swift* UVOT filters have central wavelengths (on the AB system) of $uvw2 = 1991$ Å, $uvm2 = 2221$ Å, and $uvw1 = 2753$ Å. The filter curves and a comparison of UVOT zero-points in AB and Vega photometric systems can be found in Breeveld et al. (2011) and the *Swift* CALDB.

The UVOT photometric observations in the $uvw1$, $uvm2$, and $uvw2$ filters are shown in Fig. 3 and given in Table A3. The light curve is discussed further in Section 3.7. After day 38 there could be a possible significant contribution to the UVOT aperture from the two nearby sources. To reduce that contamination to the photometry we have used a 2.5 arcsec aperture, rather than the standard 5 arcsec, with an aperture correction for count rates less than 0.5 count s^{-1} ($uvw1 < 19.72$ AB mag). The nearby stars, which fall within the UVOT PSF, are faint in the UV and no evidence of flattening of the UV light curve is found.

3.7 The slope and breaks in the light curves

The light curves are shown on a logarithmic time-scale to illustrate the temporal breaks in Fig. 3 while the rapid decline is more apparent in the linear plot, see Fig. 2. The light curve appears to consist of a few sections each with its own power law.

For the *I*, *R*, *V*, and $uvw1$ light curves we fit a function linear in magnitude, but logarithmic in time, which is equivalent to a power-law fit of flux(time) since magnitude is essentially a logarithm of the flux: $m = c - s \times \log_{10}(t)$, with c a constant, m the magnitude, s the slope, and t the time. We do that initially on each section and band, find the break times from the intersections of the power laws, whereafter we repeat the fit per section. The intrinsic variability, see Fig. 3, which is also present during quiescence, makes fitting any smooth curve difficult; the measurement errors are much smaller than the variability. There appears to be a slight change in the light curves going from the red *I* band to the ultraviolet, particularly

⁶<http://purl.com/net/mpfit>

⁷http://heasarc.gsfc.nasa.gov/docs/heasarc/caldb/swift/docs/uvot/uvotcaldb_sss.01b.pdf

Table 2. Optical–UV light-curve-fitted parameters.

Band	Start time (d)	t_{break} times				Slope see (1)					End time (d)
		t_a (d)	t_b (d)	t_c (d)	t_d (d)	s_a	s_b	s_c	s_d	s_e	
I, I_c^3	0.81	6.2 ± 0.5	9.3 ± 0.4	21.2 ± 1.9	32.0 ± 3.4	3.6 ± 0.4	16.1 ± 0.4	0.9 ± 0.5	5.1 ± 0.3	2.1 ± 0.4	100
R	2.65	5.8 ± 0.3	9.5 ± 0.3	19.9 ± 1.9	34.7 ± 7.3	3.9 ± 0.4	13.1 ± 1.5	1.3 ± 0.6	5.8 ± 1.4	2.5 ± 0.3	93
V	2.65	6.1 ± 0.3	9.2 ± 0.3	19.6 ± 1.7	29.7 ± 9.6	2.4 ± 0.7	14.6 ± 1.4	0.6 ± 0.7	6.8 ± 3.5	2.8 ± 0.3	93
B	2.64	5.8 ± 1.2	9.5 ± 0.7	19.6 ± 2.1	34.7 ± 6.8	2.1	11.0 ± 1.1	0.9 ± 0.3	5.7 ± 0.7	1.9 ± 0.3	92.6
$uvw1$	2.88	6.1	9.8	14.5	22.5	3.9	11.4 ± 0.3	0.8	6.0	3.1 ± 0.5	86
joint ²	0.81	6.5 ± 0.2	9.2 ± 0.1	19.3 ± 0.7	38.3 ± 2.7	3.6 ± 0.3	15.4 ± 0.5	1.2 ± 0.3	5.4 ± 0.4	2.2 ± 0.2	320

(1) We fit $\text{mag} = \text{constant} - s_i \cdot \log_{10}(\text{time})$, beginning at the start time with slope s_a up to break time t_a , then continuing with s_b , until t_b , etc.

(2) The joint fit of I (OGLE) I_c R_c V , B (SMARTS) $uvw1$ $uvm2$ $uvw2$ (UVOT); $uvm2$ extends to 320 d.

(3) normalized at $t = 1.0$ d the constant for each band is $I = 11.26$, $I_c = 11.36$, $R_c = 11.37$, $V = 11.67$, $B = 11.70$, $uvw1 = 11.43$; all with ± 0.15 mag, and $uvm2 = 10.95 \pm 0.35$, $uvw2 = 11.66 \pm 0.27$ mag.

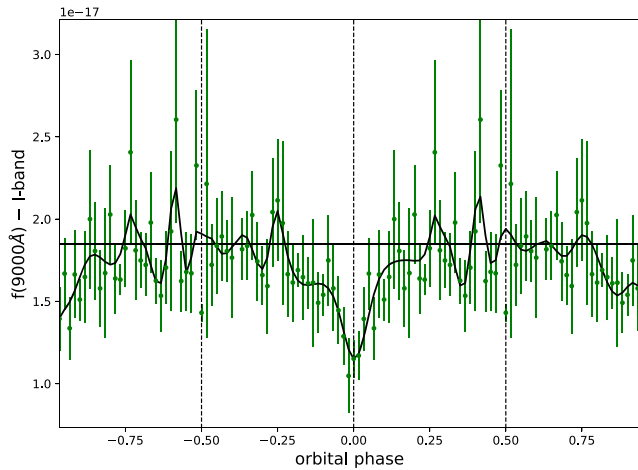


Figure 4. The I -band data folded and binned over the orbital period. The horizontal line is the mean flux for phase 0.25–0.75. The B-spline fit suggests an initial drop in brightness at phase -0.2 , a further drop at phase -0.07 , and a depth of the occultation of 0.40.

noticeable in the second slope s_2 , but generally the variabilities are so large that assuming the same evolution takes place in all bands seems acceptable. The residuals of the fit for the I , R , and $uvw1$ bands in Fig. 3, middle panel, show visually the slight differences as compared to the overall evolution. The overall light curve shows several well-separated intervals, and the joint fit in Table 2 is a good representation for those. A possible explanation of the similar light curves from the UV to the IR is that the ejecta and possibly a central source are evolving as a whole because the ejecta are optically thin, while the source remains at a nearly constant temperature. This is surprisingly different from the colour evolution in CN V959 Mon (Page et al. 2013) which forms dust and in RN V745 Sco (Page et al. 2015a) which has a red giant secondary. The main difference may be the size of ejected mass.

Schaefer (2010) has pointed out that a large number of (possibly all) RNe show light curves with distinct plateau phases like we see in N LMC 1968, and suggests that as a defining characteristic of RNe. Pagnotta & Schaefer (2014) used this in a later paper in an attempt to uncover missed RNe. The plateau onset often coincides with the unveiling of the SSS.

We combined all available 2016 and 2010 V light curves from day 2 to 6 to estimate the rate of decay. When extrapolating the fit back to the estimated eruption times we obtained values of $V = 12.3 \pm 0.5$ at eruption, and derive $t_2 = 4.6 \pm 0.5$ d and $t_3 =$

7.0 ± 1.0 d, consistent with Munari et al. (2016) and slightly slower than in I .

3.8 Periodic photometric variability

The OGLE project also monitored the nova (2010–2016) whilst in quiescence. Its quiescent mean magnitudes are $\langle I \rangle = 19.29$ mag, $\langle V \rangle = 19.70$ mag and colour $\langle V - I \rangle = 0.41 \pm 0.06$ mag. Furthermore, a periodic variation (Sekiguchi et al. 1990) is seen which is interpreted as being caused by the orbital variations (see Mróz et al. 2014, for a periodogram). Henceforth we will adopt that interpretation. We obtained an optimal period of 1.264329 d using the analysis of variance (AOV) statistic method (Schwarzenberg-Czerny 1996) using the 2010–2016 OGLE photometry, excluding the eruptions. The ephemeris was subsequently calculated using the O–C (observed – calculated) diagram. The cadence of the observations, at 1–2 d, is close to the orbital period, limiting the accuracy of the ephemeris.

The solution for the ephemeris for the primary minimum in the I band is

$$\text{HJD}_{\text{ecl}} = 2455058.323 \pm 0.090 + (1.264329 \pm 0.000019) \times N, \quad (2)$$

where the errors are 1σ . The main eclipse duration is about ± 0.07 in phase and about 0.6 mag deep (a 40 per cent decrease in flux) in the I band, see Figs 4 and 5. The short deep eclipse would be consistent with the WD being eclipsed.

We used the AOV method with the available data from OGLE and SMARTS starting from 23 d past the 2016 eruption (see Table 1) to determine if a period change could be detected, but we were unable to detect significant changes down at the ± 0.003 d error level.

Given the orbital period as derived from the I band and using the ephemeris from equation (2) we binned and folded our other photometry. We combined the V - and I -band photometry from OGLE and SMARTS, removing the first 50 d after the eruptions, leaving 559 data points. For V (107 data points) and B (64 data points) we also included SMARTS data from day 10 after the rapid decline stopped, while removing the trend. For the R (52 data points), the UVOT $uvw1$ (58 data points), $uvm2$ (25 data points) and $uvw2$ (14 points) bands we used data from the period of 10 days until 100 days after the 2016 eruption, again removing the trend. However, the average depth and width of the minimum are only well determined in the I band, and appear of similar depth in the other bands.

In 2016 December (days 315–320) we obtained, during 4 *Swift* observations of the nova system, 10 exposures in the UVOT $uvm2$

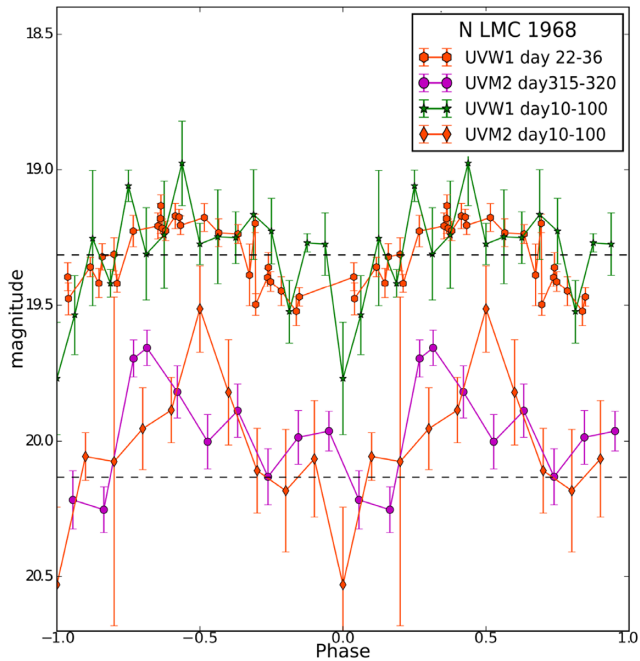


Figure 5. Light curves folded on the period of 1.264 d. On the top the average *uvw1* from days 10 to 100 has been compared with day 22–36 (the time the soft X-ray emission peak). The minimum is shallow and broad. The bottom two curves compare the average for the *uvm2* (2246 Å) band from days 10 to 100 compared with the light curve from day 315 to 320 after the eruption. The differences are due to variability. The dashed line is the average magnitude for each period.

band only. The phased *uvm2* light curve shows an asymmetry but that is due to variability during the observation. This has been illustrated in Fig. 5 where the data are for days 46–89 (labelled days 10–100). The variability in *uvm2* appears to be mostly gradual and progressive, suggesting there slow changes in the occultation of the inner system continue long after the WD luminosity returned to the inter-eruption value.

In the *uvw1* the phased light curve for days 22–36 the occultation starts around phase -0.2 , similar to the initial drop seen in the *I*-band B-spline fit. While the SSS phase was still on-going the *uvw1* shows nearly the same sinusoidal profile as the long-term average which suggests the presence of an accretion disc by day 28, see Section 5.3.

3.9 Optical spectroscopy

We obtained a series of spectra at Las Campanas Observatory (LCO) of the 2016 eruption of N LMC 1968 starting with a 120 s exposure on 2016 January 24.0345 (JD 2457411.5345, day 3.95) using the IMACS Short-Camera instrument on the 6.5m Magellan-Baade Telescope (Di Mille, Angeloni & Morrell 2016). We obtained 600 s + 2 × 1200 s long exposures on 2016 February 8, and 3 × 1200 s on 2016 February 9 and 10 (days 19–21) on the 2.5m du Pont telescope using WFCCD/WF4K-1, and finally exposing for 900 s on March 29 (day 68) with the IMACS Short-Camera, see Table A1. Spectral resolution is ~ 5 Å for the IMACS data, and ~ 8 Å for the WFCCD. We used standard IRAF routines to reduce the LCO spectra of the nova as well as those of spectrophotometric standard stars observed on the same nights for the flux calibration.

The first 2016 spectrum shows a moderately blue continuum dominated by broad Balmer, He I (triplet) and He II emission lines,

see Fig. 6. The lines have an FWZI of about $10\,000\text{ km s}^{-1}$, implying velocities of 5000 km s^{-1} and present jagged profiles. A bright narrow emission peak at a velocity of $\sim 1600\text{ km s}^{-1}$ is clearly visible on the blue edge of the Balmer and He I lines, but there is no narrow centred component on the lines as seen day 8 and later. The He II 4686 Å line appears to have a more symmetric profile, which is due to a blend with the Bowen C III and/or N III lines.

A spectrum (4000–7200 Å) was obtained on 2016 January 28 starting at 10:17 UT (day 8.0, phase 0.73) with 11 × 300 s exposure at the Mirranook Armidale site using a LISA spectrograph on a C11 telescope with a 23 μm wide slit (about 3 arcsec on the sky). The spectrum shows the H α, H β, and He II 4687 Å lines, and the lines feature narrow components.

Further spectra were obtained using the FLOYDS instrument⁸ on the 2.0m Faulkes Telescope South at Siding Spring Observatory, NSW, Australia on 2016 January 29.6 UT (JD 2457417.1, day 9.2, orbital phase 0.63). We obtained a series of spectra 3 × 900 s long. The spectral range covers 3200 Å to 1 μm at a resolution of $R \approx 550$. The signal-to-noise of the combined spectrum is particularly low and only four emission lines are clearly visible, H α, H β, He II (4687 Å), while the He I lines are no longer seen. The H α line consists of a bright narrow central peak with FWHM = $1900 \pm 100\text{ km s}^{-1}$ on top of a broader pedestal with FWZI $\approx 10\,000\text{ km s}^{-1}$. We calibrated the spectrum using the mean fit to the photometry given in Table 2.

In Fig. 6 the SAAO spectra from the 1990 eruption also show a centred narrow-line component on day 8.78 and 15.73 similar to that seen in 2016, but the underlying broad ‘pedestal’ of the line profiles shows a different profile in 2016 than in 1990.

Table A1 gives an overview of all the spectra, including the orbital phase.

3.10 Swift UV spectroscopy

Daily *Swift* UVOT UV grism spectra were obtained between 2016 January 23 06:40 UT (day 2.875) and 2016 January 29 (day 9).

The first grism observations consisted of two 500 s segments with different roll angles in order to have a different zeroth order contamination from field stars. The details of the UVOT spectra have been given in Tables A1 and A2. The spectra were processed using the calibration of Kuin et al. (2015) and code described in Kuin (2014). The calibration used includes the 2017 update to the sensitivity loss which affects the spectra below 2000 Å.

After extraction, the UVOT spectra were validated since the UVOT grism images need careful analysis (see Shore et al. 2018, for details). The grism images were compared to the star field and contaminating zeroth orders were flagged. This was especially important for the first six spectra because no offset on the detector was used (see Table A2).⁹ Though the UV grism spectrum from day 6.14 (phase 0.22) was unusually bright when compared with the longer term trend, it was found to be consistent with the photometry taken right before and after the spectrum showing that a brightening was taking place at that time. In order to correct for errors in the wavelength fiducial point (the anchor point, see Kuin et al. 2015) which applies equally to all spectra on a grism image, spectra of

⁸<https://lco.global/observatory/instruments/floyds/>

⁹The advantage of using an offset position on the detector around (1000,1600) is no second-order overlap while zeroth-order contamination is restricted to below 2000 Å.

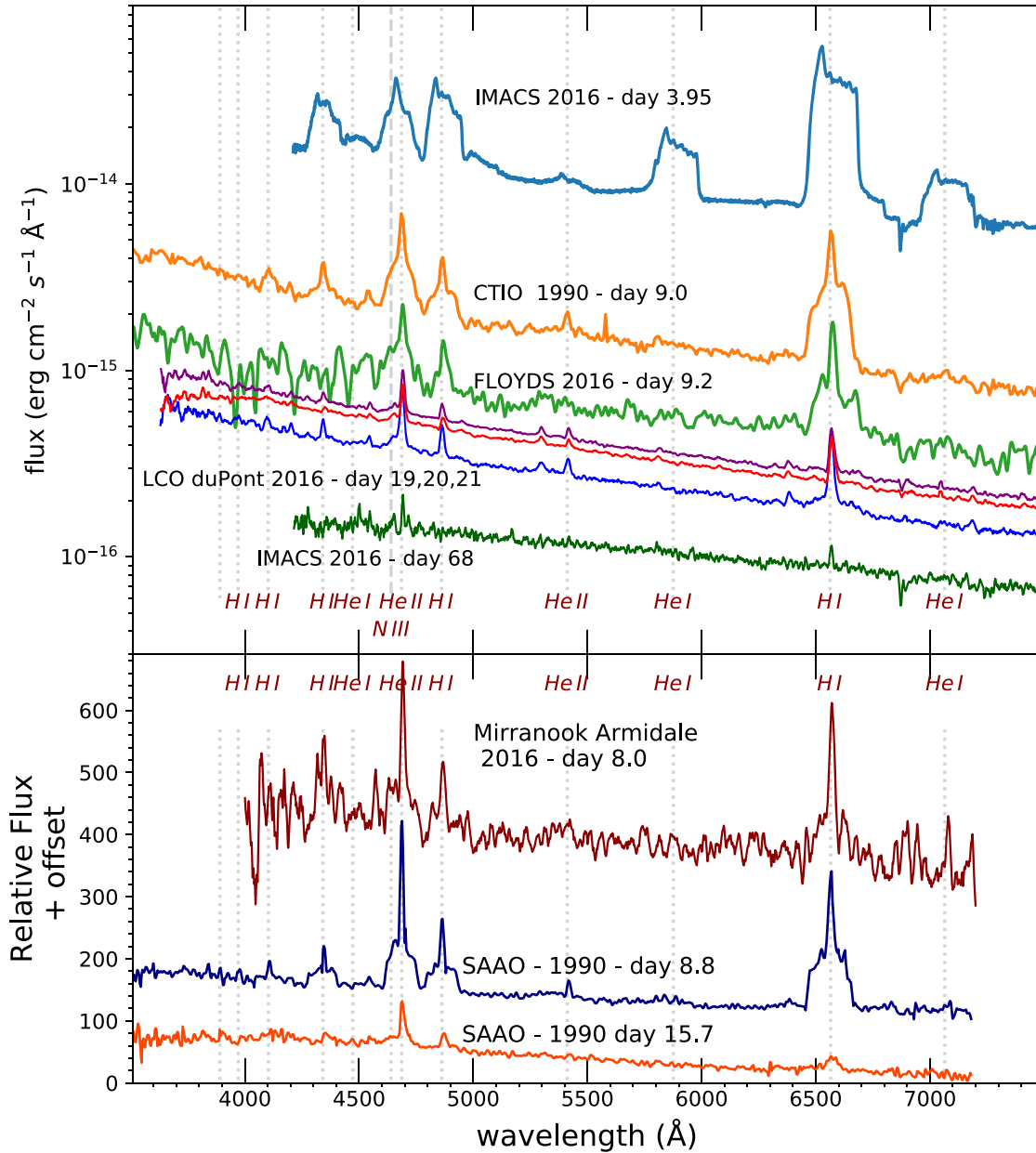


Figure 6. The optical spectral evolution of the nova in 1990 and 2016. The spectra in the top panel have a flux calibration, those in the bottom panel are not flux calibrated. We show the optical spectra from the 1990 and 2016 eruption.

a bright nearby F5 star were extracted and used to determine a correction.

The spectra were very noisy, so we summed them to enhance the UV line emission. However, it was clear that spectra near phase 0.5 were different, while the other spectra were essentially the same, so these were summed separately. In Fig. 7 the spectra near phase 0.5 have been shown together with earlier and later summed spectra. We found weak broad lines of He II 2734 and 3204 Å, consistent with the optical spectra. A bright line appears to be present at ~ 1909 Å due to C III]. We were unsure if the loss of flux below 1850 Å in all spectra is due to absorption or to the calibration of the sensitivity loss which is particularly difficult where the response falls to zero. We also noted a broad line which we identify as the Bowen O III 3133 Å line which is pumped by He II, consistent with the appearance of the C III/N III Bowen lines at 4630–4650 Å. Since

we do not see strong UV line emission, the ejecta are not in the nebular phase before day 9.

3.11 *Swift* XRT spectra

Spectra were extracted for each individual snapshot of XRT data (where a snapshot is a continuous *Swift* pointing) after the soft emission became evident (with the first good soft X-ray spectrum for day 7.2), except for data after day 33, where several observations were combined to get spectra of sufficient signal-to-noise. A single spectrum was also extracted for the early, pre-supersoft-source (SSS) emission (days 2.9–6.1). The spectra were binned to a minimum of 1 count bin^{-1} in order to facilitate fitting using the Cash (1979) statistic within XSPEC.

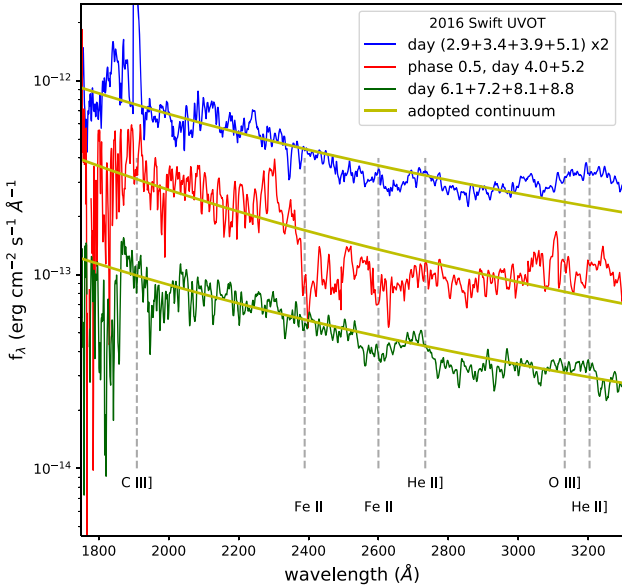


Figure 7. The observed Swift UVOT UV spectrum. The spectra were summed to improve S/N, weighted by the flux error. Since the early spectra are brighter, they will tend to dominate. The spectra past day 6 were taken at an offset and do not suffer from second-order overlap which raises the continuum level in the earlier spectra above 2800 Å. A power law continuum has been fit to illustrate the presence of Fe II absorption features which are more prominent at phase 0.5, days 4–5.2. There are many Fe II lines in the 2380–3020 Å band; the UV 1 and 2 multiplet locations have only been indicated. A reddening correction for $E(B - V) = 0.07$ was applied to the spectra, see Section 4.3 and the earliest spectrum was multiplied by two for clarity. The spectra show lines of He II 2734, 3204, O III] 3133, and C III] 1909 Å.

We can expect that prior to the rise in SSS emission on day 6 the ejecta are optically thick for X-ray emission from the WD below, and the hard X-ray spectrum is due to the optically thin emission in a shock in the ejecta. After day 6 the ejecta become transparent and the WD photospheric emission shows through. Between day 6 and the time that the X-ray emission peaks around day 14 we expect the column density to include a decreasing contribution from the ejecta above that from the ISM. At late times, absorption from the ejecta will be negligible, and we can use that to derive the ISM column $N_{\text{H-ISM}}$ from modelling our XRT spectra.

We start with determining the ISM N_{H} by modelling the late-time spectra, day 21 and onwards. From our late-time models we derive $N_{\text{H}} = 1.8 \times 10^{21} \text{ cm}^{-2}$. We can compare this to the LAB (Kalberla et al. 2005) 21 cm survey, separating the LMC and Galactic components, and using the total velocity range, -150 to $+300 \text{ km s}^{-1}$ the column $N_{\text{H-ISM}} = 1.8 \times 10^{21} \text{ cm}^{-2}$ within a 0.27 beam.¹⁰ The model value is thus consistent with the interstellar one.

The early, day 2.9–6.1, spectrum was fitted with an optically thin thermal component (APEC), with $kT = 5.5^{+19.1}_{-2.6} \text{ keV}$, and N_{H} fixed at the late-time value. The 0.3–10 keV unabsorbed luminosity of this early hard component is $1.9^{+0.7}_{-0.5} \times 10^{35} \text{ erg s}^{-1}$ which is lower than the (later) soft X-ray luminosity. The model has been chosen as appropriate for shock-heated plasma emission from internal shocks and was assumed to be unabsorbed by the ejecta.

During day 6–14 we observe a rise in the XRT count rate due to the increase in the soft component. Since there are very few counts

above $\sim 1.5 \text{ keV}$ after day 6, a model consisting of an absorbed blackbody (BB) component was sufficient to parametrize the SSS spectra. While a WD model atmosphere, such as the Tübingen Non-Local Thermal Equilibrium Model Atmosphere Package (TMAP¹¹) would be more physically appropriate, the temperatures required by these XRT spectra were typically too high for these model grids. We assume that the SSS emission originates from the hot WD photosphere and that the rise in SSS is due to the ejecta becoming transparent as proposed by Krautter et al. (1996) and Shore, Starrfield & Sonneborn (1996). We make the further assumption that the WD X-ray luminosity is constant from the eruption until the end of the SSS phase (Krautter et al. 1996). We find the bolometric luminosity of the soft X-ray source by using the mean value during the SSS plateau from a fit with N_{H} fixed to the ISM value during day 20–30, i.e. $L_{\text{X-Bol}} \approx 1.1 \times 10^{37} \text{ erg s}^{-1}$, and use that for the model prior to day 14 when N_{H} is high.¹² During day 6–14 we assume N_{H} includes an additional component due to the optical thickness of the ejecta and fit a blackbody model leaving N_{H} to vary with a lower limit set by the interstellar medium value $N_{\text{H-ISM}}$. The result is shown in Fig. 8 where we see that indeed the column density shows a steep decrease from $N_{\text{H}} > 4 \times 10^{21} \text{ cm}^{-2}$ to the ISM value over approximately a 3 d period prior to the SSS ramp up. Using the fitted blackbody temperature ($\sim 100 \text{ eV}$) and the fixed luminosity ($1.1 \times 10^{37} \text{ erg s}^{-1}$), we derive a BB radius of $\approx 3270 \text{ km}$ for the hot photosphere of the WD during the peak SSS emission. There are some caveats: (1) the assumption of a BB spectrum may not be valid and the temperature may not have the usual physical meaning; (2) the system is eclipsing, so the rim of the accretion disc may hide part of the WD emission; and (3) the theoretical radius of a $1.3 M_{\odot}$ WD is smaller than 2800 km (Carvalho, Marinho & Malheiro 2018), which suggests the error in the blackbody temperature estimate is of order 8 per cent.

Fig. 9 shows a comparison of four spectra obtained throughout the rise to peak count rate. The first spectrum, up to day 6, is hard, as described above. On day 7.2 the ejecta have started to clear though the value of N_{H} still exceeds the ISM value. Despite the count rate being very similar before and after the pole constraint gap, days 14.1 and 24.1 show very different spectral shapes. The BB fit shows the later spectrum being about 20 eV hotter. That suggests that the radius of the WD photosphere decreased by about 30 per cent between day 14 and day 24.

In Fig. 8 the fitted luminosity is found to be an order of magnitude lower than the Eddington luminosity for a $1.3 M_{\odot}$ WD, which is $1.6 \times 10^{38} \text{ erg s}^{-1}$. The spectral hardening on day 24.1 takes place at the end of the plateau in the optical light curves which break around day 19.3, see Table 2. Assuming a blackbody spectrum for the SSS source the soft X-rays do not contribute significantly to the UV-optical emission. Therefore, to derive the bolometric luminosity the contemporary UV-optical/IR emission needs to be added to the L_{x} from the BB fit. We come back to the luminosity in Section 5.6.

3.12 IUE, CTIO, and SAAO data of the 1990 event

The International Ultraviolet Explorer (IUE) spectra we retrieved are from the IUE Final Archive which improved upon the earlier

¹¹http://astro.uni-tuebingen.de/rauch/TMAF/flux_HHeCNONeMgSiS_gen.html

¹²The modelling choices made here are made because the fitted parameters are not completely independent, and optimizing just on the goodness of fit may result in unphysical values

¹⁰<https://www.astro.uni-bonn.de/hisurvey/profile/index.php>

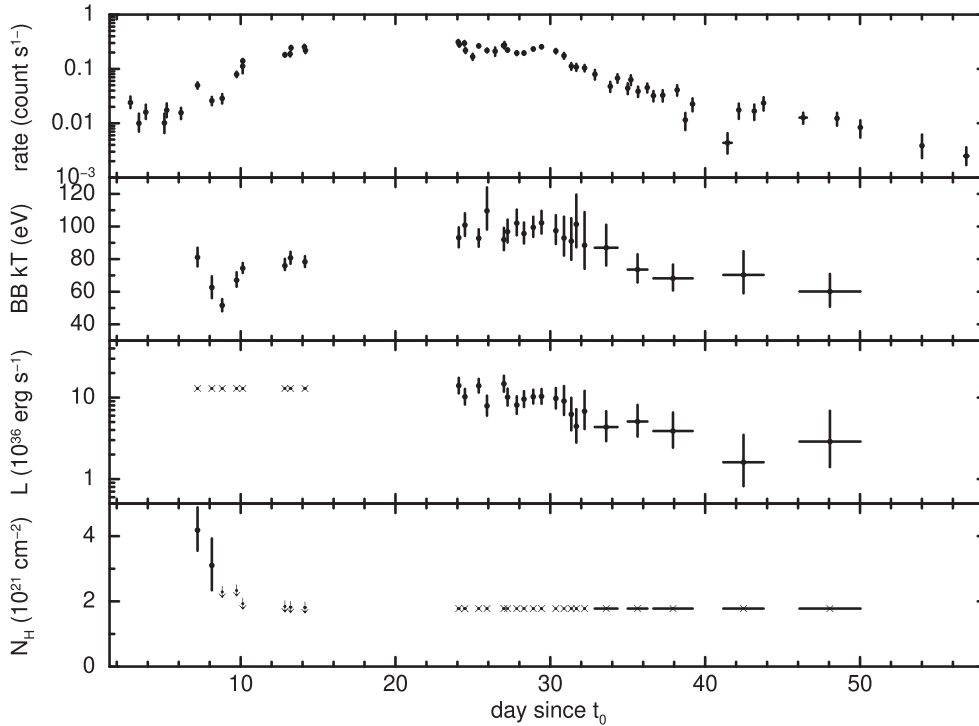


Figure 8. Top panel: The observed light curve over the full XRT band (0.3–10 keV). Second panel: The temperature of the blackbody fit to the soft spectrum. Third panel: For times > 14 d: The estimated bolometric luminosity of the BB, assuming a distance of 50 kpc; for early times L_x has been set to the mean from day 20 to 30. Fourth panel: Prior to day 14: the estimated NH column. After day 14: the adopted N_{HISM} value based on a fit to the spectra past day 20.

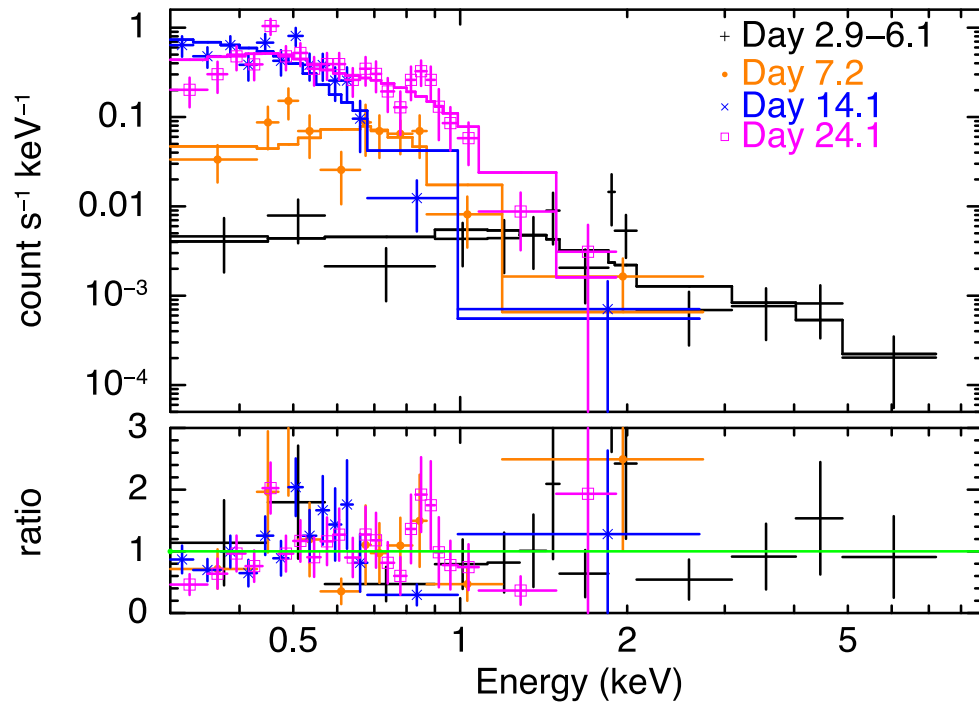


Figure 9. A sample of the Swift-XRT spectra fitted with a BB model. The lower panel shows the ratio between the data and model.

spectral extraction (Nichols & Linsky 1996), see Fig. 10. The long wavelength (LWP) *IUE* spectra cover 1900–3200 Å, comparable to the UVOT UV grism, but suffer from much noise and weak emission lines. The strongest line often seen is C III]. The shorter *IUE* wavelength band (SWP) contains strong emission lines from

C, N, and O, and H Ly α . For the *IUE* spectra, as well as the spectrum of N LMC 1990b taken with the 1.9 m telescope at the South African Astronomical Observatory (SAAO) in Sutherland and for the spectrum which was taken at the Cerro-Tololo Inter-american Observatory (CTIO) we can use the OGLE ephemeris

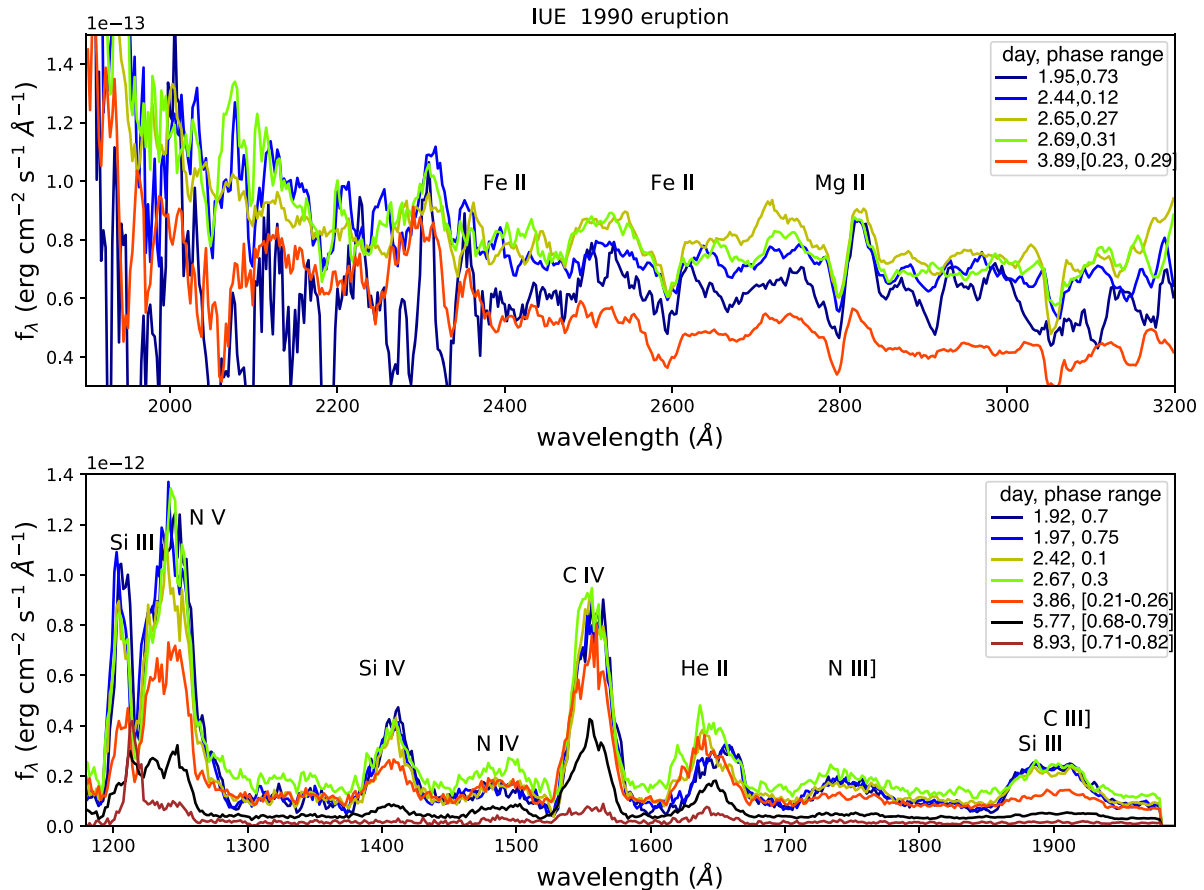


Figure 10. The *IUE* long (LWP) and short (SWP) wavelength spectra from the 1990 eruption. Phase is from our ephemerides. The LWP spectra show absorption of Fe II and Mg II. The LWP emission lines have been indicated. No reddening correction was applied.

from equation (2) for attaching an orbital phase to the 1990 outburst observations with an uncertainty of ≈ 0.15 in phase derived from the uncertainty in the ephemeris, see Table A1. With this uncertainty in the assigned phase for the 1990 observations in mind, we proceed to use them in our interpretation of the nova.

4 OBSERVATIONAL RESULTS

4.1 The companion star

Mróz et al. (2014) suggested that the period can in principle be twice that given above. However, the UV spectrum at phase 0.5, day 4 and 5.2 showed an increase in Fe II absorption. Though this is due to an ionization effect (see Section 4.5), it could also be associated with extra mass present outside the L2 point. The orbital period suggests that for a Roche lobe filling secondary, the secondary must be evolved (Shore et al. 1991; Mróz et al. 2014).

We checked the pre-eruption WISE IR data for insight into the contribution from the companion. However, a comparison with the higher resolution OGLE image, see Fig. 1, shows that there are two sources within 3 arcsec of the nova, less than the 6.1 arcsec resolution in WISE Band W1 and the 6.4 arcsec resolution of Band W2 so that no useful information can be obtained on the companion from WISE data.

The 2016 February 19, 20, and 21 LCO spectra cover the 3800–9000 \AA band at phase 0.98, 0.76, and 0.51, respectively. This was

at the end of the plateau in the light curve. To adjust for the brightness changes we scaled the spectra using the flux of the H α line which is formed in the ejecta. We see at phase 0.51 the whole WD-facing atmosphere and at phase 0.76 only half. After scaling the spectra at phase 0.76 and 0.51 are identical within the error, so we do not observe any difference in emission due to the heated atmosphere on the side of the secondary facing the hot WD. From these observations we derive a $3\text{-}\sigma$ flux limit for the heated atmosphere in the secondary is less than $1.1 \times 10^{-13} \text{ erg cm}^{-2} \text{ s}^{-1}$ which is negligible.

The slope of a power-law fit to the LCO spectrum on day 20 is 2.27 ± 0.03 , close to what an α -disc model predicts, supporting that the accretion disc was present.

4.2 The mass of the WD

The luminosity–temperature relations in both Sala & Hernanz (2005) and Wolf et al. (2013) show that a peak temperature of $>100 \text{ eV}$ implies a high WD mass of $>1.3 M_\odot$. Compared to CN eruptions, RNe have much shorter intervals during which material can be accreted on to the WD, and less is needed to get ignition. Therefore, there is less material ejected during the eruption of a recurrent system. Supersoft X-rays will only be observable when the ejecta have become optically thin (e.g. Krautter et al. 1996), therefore RNe and, by extension, high-mass WDs, are expected to have both short turn-on and turn-off times for their SSS phases.

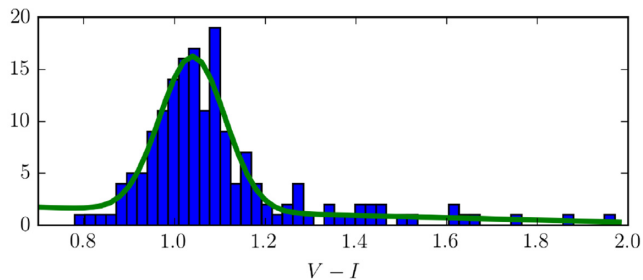


Figure 11. The histogram of the $V - I$ colour for the red clump in the colour–magnitude diagram of the 2 arcmin \times 2 arcmin region around the nova.

This is indeed found to be the case for N LMC 1968, with turn-on and turn-off times of about 7 and ~ 30 d, respectively. These times are completely consistent with the correlations found by Henze et al. (2014a) when analysing a sample of M31 novae. The earliest detection of a SSS so far was for V745 Sco (Page et al. 2015b), with soft X-ray emission first seen about 4 d after eruption. V745 Sco has a recurrence time of ~ 25 yr. The rapid RN M31N 2008-12a also showed an early turn-on of the SSS phase, 6 d after the nova eruption (Henze et al. 2015). The small 3270 km radius of the WD photosphere as derived from the blackbody model of the peak SSS XRT spectrum in Section 3.11 is also indicative of a massive WD with $M > 1.25 M_{\odot}$ (Carvalho et al. 2018).

4.3 Reddening

We considered several lines of evidence for determining the interstellar reddening toward the nova. We made an estimate of the reddening in the direction of the nova using the Red Clump (Girardi 2016) in the colour–magnitude diagram by centroiding on a 2 arcmin \times 2 arcmin region around the nova (30 pc \times 30 pc at a distance of 50 kpc), where the measured colour $(V - I)_{\text{RC}} = 1.02 \pm 0.01$ mag (see Fig. 11). Assuming an intrinsic colour for the Red Clump of $(V - I)_{\text{RC}} = 0.92$ for LMC metallicity, the reddening is $E(V - I) = 0.10$ mag. Assuming a Cardelli law (Cardelli, Clayton & Mathis 1989) this corresponds to $A_V = 0.21$ mag, $A_I = 0.10$ mag, and $E(B - V) = 0.07$ mag. This is consistent with NED¹³ Galactic extinction calculator which gives a visual extinction of $A_V = 0.206$. For an IR-independent estimate we take N_{H} discussed before in Section 3.11 from the XRT spectral fit and the LAB 21 cm survey; the column $N_{\text{H}} = 1.8 \times 10^{21} \text{ cm}^{-2}$. This value is consistent with the reddening and $N_{\text{H}}/E(B - V)$ ratio that has been reported for the LMC (Koorneef 1982). Using the Bohlin, Savage & Drake (1978) calibration this is $E(B - V) = 0.09$. For the Liszt (2014) calibration for $|b| > 20^\circ$, $E(B - V) = 0.07$. We adopt $E(B - V) = 0.07 \pm 0.01$ in this paper.

We can use the UV spectra to learn more of the reddening specific to this nova. Both the 1990 *IUE* LWP spectra and the *Swift* UVOT spectra cover the $\lambda 2175 \text{ \AA}$ feature from which a lower limit to $E(B - V)$ can be derived. Using the Verbunt method (Verbunt 1987) after summing all the spectra and fitting the continuum, the Cardelli et al. (1989) Galactic extinction law was applied for various values of $E(B - V)$ using $R_V = 3.1$ and visually inspected. The bump in the spectrum (positive or negative) disappeared for a very low

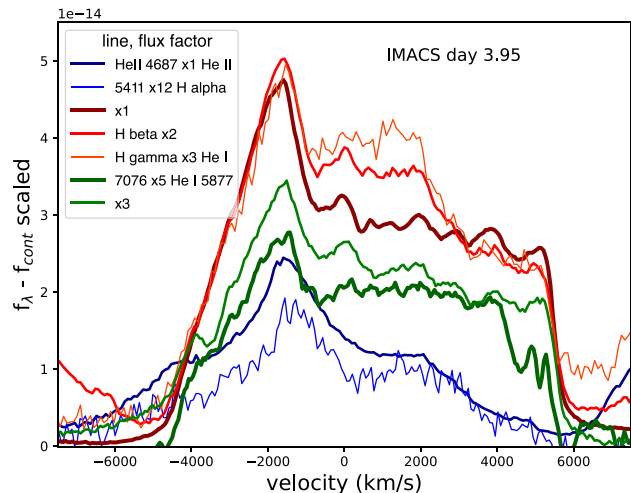


Figure 12. On day 3.95 in the 2016 outburst, the H and He line profiles in the IMACS spectrum have been displayed in velocity space. The He II lines show less emission on the red wing than the H and He I lines. Assuming symmetry, the line H and He I profile centres are at 1035 km s^{-1} .

$E(B - V) = 0.006 \pm 0.003$, suggesting the absence of the Galactic $\lambda 2175 \text{ \AA}$ feature in that direction.

4.4 The He II line profiles variations

In the early days after the eruption opacity effects may cause shadowing of the red-shifted emission originating in the receding part of the ejecta by the approaching blue-shifted part. The suppression of the positive velocities in the 2016 spectrum from day 3.95 shown in Fig. 12 suggest that this mechanism could be operating. However, there is another explanation: The 1990 *IUE* spectra, see Fig. 10, show mostly symmetric line profiles in nearly all lines except in the He II 1640 \AA line. We illustrate the evolution of the He II 1640 line profile, see Fig. 13, by normalizing to the light curve. The He II 1640 \AA profile is markedly different at orbital phase ~ 0.7 (days 1.92, 1.97) compared with phase 0.1 and 0.3 (days 2.42 and 2.67, respectively). The spectra at phase 0.7 have more emission on the red wing centred on about 1660 \AA and less on the blue wing than the spectra at phase 0.1 and 0.3. Similarly, the day 3.86 (phase 0.21–0.26) spectrum matches those of day 2.42 and 2.76 (phase 0.1 and 0.3) in peaking in the blue, but then the day 5.77 (phase 0.68–0.79) spectrum is more like the day 1.92 and 1.97 (phase ~ 0.7). The location of the peak is related to having a similar orbital phase. Such line profile changes are limited to the He II 1640 line, even though the other lines of ions with high-ionization energy (N V 1242, Si/O IV 1402/1406, C IV 1550) do not show much change to the overall profile prior to day 6, just to the flux. Hence, the asymmetric profile of He II lines in the 2016, day 3.95 (phase 0.23) spectrum may also be due to a variable component.

We conclude that in the 1990 eruption during day 2–9 the variable component of the He II 1640 emission line is tied to the orbital motion of the binary system, while the emission in H, He I, and the N III, C III, C IV, and Si IV is not; those are formed in the ejecta. After day 8 a narrow component is a new addition to the He II profile; we discuss narrow profiles in Section 4.6. The variability by orbital phase in He II is possibly related to the accretion reestablishing which we discuss in Section 5.3. This might mean that the donor star is He rich (Shore et al. 1991), or that part of the WD atmosphere is ejected during the eruption but remains bound to the system.

¹³NASA/IPAC Extragalactic Database, <http://ned.ipac.caltech.edu>, based on SDSS data

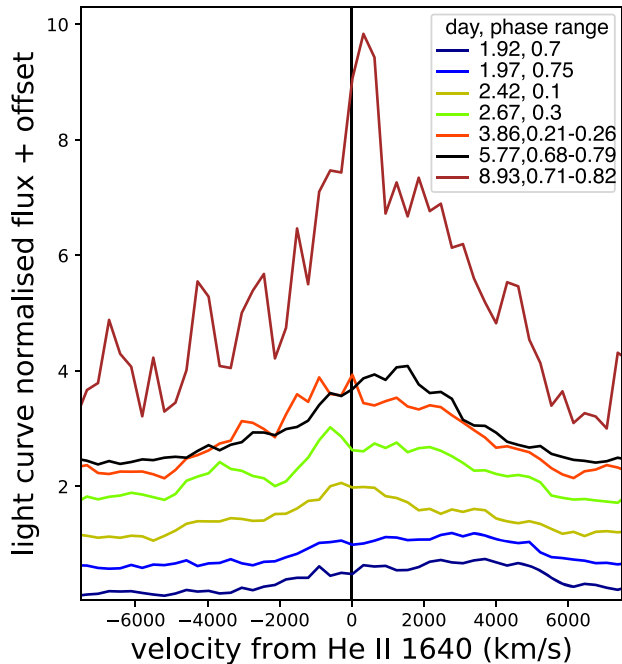


Figure 13. The changing profile of the 1990 *IUE* SWP He II 1640 line profile up to day 9. The flux has been normalized using the light-curve fit in Table 2 and offset for clarity. The He II flux did not drop as fast as the nova brightness, and thus the earliest normalized line is the weakest, and the latest is the strongest. Note that between day 5.77 and 8.93 a central narrow-line component appears. Ignoring the narrow-line profile, the broader line tends to the red for orbital phase near 0.7 and slightly to the blue for orbital phase near 0.2. These line profile changes are not seen in the spectra of neutral H and He.

4.5 The recombination wave in the Fe II UV 1 feature at 2600 Å

In the UVOT spectra (Fig. 7) we see on days 4–6, evidence for Fe II absorption with features that extend over the whole range of 2300–3100 Å. Inspection of the 1990 LWP *IUE* spectra (Fig. 10) also showed the Fe II 2600 Å line. To better understand how this absorption is formed we determined the absorption fraction under the continuum of the reddening corrected spectra in the 2550–2625 Å band. The continuum for each spectrum was fitted with a fixed slope ensuring that the continuum was applied in a consistent way, and checking that the normalized spectra matched in the spectral regions least affected by the absorption features or emission lines. The errors were determined by varying the normalization. The measured value is shown in Fig. 14 as a function of time after eruption.

The sudden strengthening of the Fe II absorption on day 4, and its subsequent decline to the previous level on day 9 is possibly due to a recombination wave. Recombination waves can be due to changes in opacity, temperature, and ionizing flux. Whilst the peak occurred around phase 0.5, earlier measurements did not match the later rise, so it is thought to be unlikely to be due to an orbital effect. After day 4 the ionizing flux from the SSS phase starts to increase and cause the Fe II absorption decrease.

During day 5.2 the overall UV flux in the spectra from 1700 to 3000 Å is lower and the *uvw1* photometry of day 5.22 is also fainter. This is probably due to the recombination wave as well.

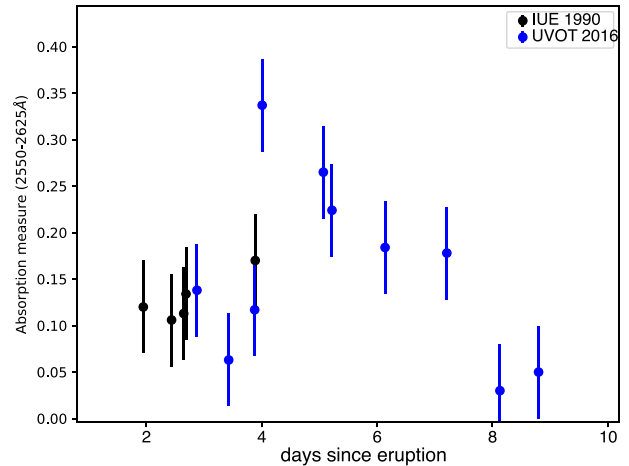


Figure 14. The relative absorption below the continuum of the region 2550–2625 Å which includes the Fe II 2600 Å resonance line. At day 4 a recombination wave occurs.

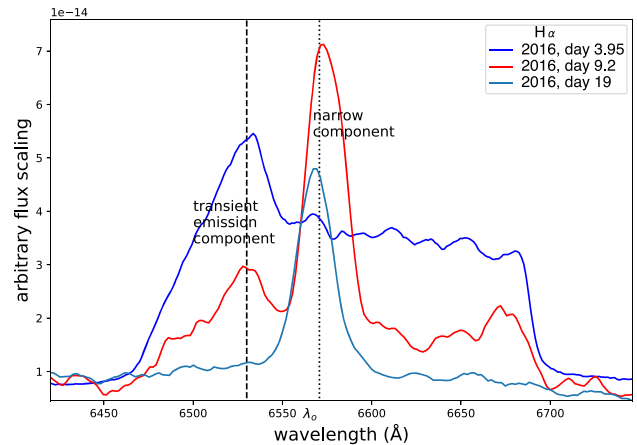


Figure 15. Sample line profile changes in H α during the 2016 eruption (for the full spectra see Fig. 6). Initially, the line is very asymmetric and skewed with a transient blue peak which is seen around day 4, and weakly day 8 (not shown). No narrow central peak is found until day 8; it is well-defined day 9.2 and it is still present on day 19. On day 68 it is no longer prominent. The spectra are plotted with observed wavelength, and the dotted line is the central wavelength of H α corrected for the systemic velocity of the LMC of 278 km s $^{-1}$.

4.6 Narrow-line profile components

In our analysis we use spectra of the 1990 and 2016 outbursts. In Figs 6 and 15 a centred narrow-line component can be seen in the H and He lines in 1990 and 2016 spectra after day 8 of the eruption and lasting at least till day 21.

A comparison of the 2016 FLOYDS spectrum (day 9.2, phase 0.63), of the 2016 spectrum from Mirranook Armidale (day 8.0, phase 0.73), of the first spectrum from Sekiguchi et al. (1990) of the 1990 eruption obtained on 1990 February 22 (day 8.73), and the 1990 CTIO spectrum of day 9.0 (phase 0.3), Fig. 6, shows that none of them exhibits any differences in the narrow component with orbital phase.

Since the Balmer decrements show that the narrow component is due to recombination, we can expect a similar behaviour both in H

and He lines and use that to determine when the narrow component appeared. Between day 4 and day 8, a 1990 *IUE* spectrum was taken on day 5.8, which can be compared to the *IUE* day 8.9 spectrum. There is a central peak present in the day 8.9 spectrum in the He II 1640 line that is not seen in the day 5.8 spectrum, suggesting that the narrow-line developed between day 6 and 8 (since we see it in the day 8 optical spectrum).

Narrow components were also seen in other short-period RNe. A well-observed sequence can be seen in Nova LMC 2009a where the narrow component is seen to appear around day 10 and disappear when the SSS phase ends and thus the X-ray luminosity drops (Bode et al. 2016).

Williams et al. (1981) describe *IUE* observations of the 1979 outburst of nova U Sco where He II 1640 developed a narrow component between day 6 and 8 after discovery. Sekiguchi et al. (1988) display a sequence of spectra for the 1987 outburst which shows no narrow peak on day 4, but it is present on day 9 and 19 after eruption. The well-observed 2010 eruption shows that on day 5 there was no central narrow component (Kafka & Williams 2011; Mason et al. 2012), while it is present on the day 5.8 spectrum and disappeared between days 33 and 41 (Anupama et al. 2013), comparable to the end of the SSS phase around day 40 (Orio et al. 2013).

RN V394 CrA, a fast nova showing similarities to U Sco, had two outbursts, one in 1947 (Duerbeck 1988), and one in 1987 (Liller et al. 1987). Spectra taken on 1987 August 3 and 4, 5, and 6 days after the eruption show only a broad flat line profile in the H I and He II lines, while by 1987 August 13, day 11 and later, they show a narrow-line profile component in these lines which appears diminished by September 15. A spectrum taken 1987 October 4 shows that the narrow component has all but disappeared (Starrfield et al. 1988a; Sekiguchi et al. 1989).

The narrow lines are thus found in similar RNe systems, and are characterized by the initial absence until several days after the eruption, and disappearance at the time the SSS emission also drops off. This suggests that the narrow emission is powered by the high-energy emission from the WD, just like the soft X-rays are.

Several mechanisms have been proposed to explain these narrow lines centred on the line wavelength and on top of a broad pedestal. Almost certainly the narrow component of the line is formed in a different region from the broad pedestal which is due to the ejecta. We explore the possibility here, that the narrow component is due to reionization of trailing clumps of cool matter from the previous eruption at distances of several 10^{16} cm. The time delay between the eruption and the appearance of the narrow lines is due to the light traveltime to reionize the distant shell, assuming the UV/EUV radiation from the photosphere is sufficient even before the start of the SSS phase. The observed line width (FWHM) of $\approx 1100 \text{ km s}^{-1}$ will be due to a low gas temperature and velocity of the clumps, and is consistent with the distance reached in about 7 yr by the slower ejecta. The recombination time needs to be less than about a day which requires densities of $>10^7 \text{ cm}^{-3}$ and implies a filling factor of $<10^{-6}$. Estimated filling factors in the days after the eruption of 0.01–0.001 scale after 7 yr of expansion to $<10^{-6}$ provided the clumps do not grow faster than by thermal expansion.

We cannot reliably detect variations in the narrow component with orbital phase in N LMC 1968. Reionization of clumpy ejecta from a previous eruption provides a possible explanation for the narrow-line profiles.

5 OBSERVATIONS IN A MODEL CONTEXT

5.1 A comprehensive model

Late-time spectral observations show that nova ejecta have a bipolar shape (Mustel & Boyarchuk 1970; Hutchings 1972; Solf 1983; Gill & O'Brien 1999, 2000; Harman & O'Brien 2003; Ribeiro et al. 2009; Shore 2012; Shore et al. 2013a,b, 2016), and we will assume this to be so for this nova. The visible brightness decay time-scale t_3 is shorter for smaller mass ejected and higher velocity since the ejecta become transparent faster. In the RNe with a late-type secondary the SSS X-ray emission onset is delayed from the eruption itself by a period of at least a few days (Schwarz et al. 2011). The SSS emission is likely the surface emission of the WD with nuclear burning continuing after the initial eruption for a period of weeks to months until the all the hydrogen has been burned. The upper atmospheric temperature of the WD is typically $<1 \text{ MK}$.

The accretion disc may have been disrupted in the initial eruption (for U Sco, see Drake & Orlando 2010), though the ejected mass is low, reducing the potential for disruption. For example, in M31 N 2008-12a the accretion disc is thought to survive (Henze et al. 2018). In addition to the eruption, the high luminosity of the WD will heat the atmosphere of the secondary. For a secondary that fills its Roche lobe this leads to matter filling the inner WD Roche lobe from both the accretion disc and by overflow from the heated atmosphere. Eventually that matter will undergo a pancake-like instability and reform the accretion disc. At the same time, over possibly a long period, hydrogen is converted to helium in the layers still bound to the WD, and not lost.

Thus, in the higher mass WDs ejecta become transparent faster, reducing the time for the density of the ejecta to become low enough to observe the WD and inner system. N LMC 1968 has a very small t_3 , smaller than the Galactic nova U Sco which also has an evolved companion, similar spectra, and SSS phase, and a comparable orbital period of 1.23d (Schaefer & Ringwald 1995). In N LMC 1968 the suggestion of the changing eclipse profile, the early occurrence of eclipses, and the behaviour of He II (see Section 4.4) are all consistent with a model where debris filling up the inner WD Roche lobe initially block the WD photosphere from view, though that does not rule out that the bipolar ejecta also cross the line of sight. We will consider the consequences of that in the following subsections.

5.2 Inclination of the orbit

It is likely that we are seeing the system at an inclination angle close to the orbital plane because we have seen eclipses. Ness et al. (2013) estimate an inclination angle of $>76^\circ$ is to be expected for an SSe type system (which shows emission lines). Our interpretation of the UV flux variations suggests that we view close across the rim of the accretion disc, which would imply a system inclination in the $68\text{--}76^\circ$ range: Fagner & Nelson (2010) show that for a low α , thicker disc, the disc can warp and rotate rigidly, which could fit with the observed changes to the UV emission.

The SSS onset could be expected to happen sooner if the line of sight were not intersecting the bipolar ejecta, i.e. at high inclination. The presence of an accretion disc does not preclude scattering of soft X-rays in a halo above the disc. However, in such a situation the debris left in the inner Roche lobe in the days after the eruption could effectively block the X-rays and delay the SSS onset.

5.3 The accretion disc and precursor

It is unknown what happens to the accretion disc during and after the nova explosion, but N LMC 1968 may provide some insight. The main questions relating to the accretion disc are: (1) was the accretion disc destroyed in the explosion, (2) does the Roche lobe overflow (RLOF) from the secondary change, and (3) how long until the accretion disc is restored as a steady element in the system? The hydrodynamic models from Drake & Orlando (2010) show that in the eruption of U Sco, a very similar system, the accretion disc would not survive the initial blast which seems to answer point (1). However, we do not have the data to support that. The accretion disc may very well have survived the blast; perhaps in a state where the vertical structure was no longer in hydrostatic equilibrium. As to point (2), our observations show evidence of matter bound to the system in the UV variability, in the changes to the He II profiles as early as day 2, and RLOF is possibly a factor in the delay of the onset of the SSS. As to point (3): if indeed the 'debris' is sufficiently spread out throughout the inner Roche Lobe and neighbouring regions, that matter, whilst blocking the X-rays from the WD atmosphere, would need to collapse to the orbital plane to reform the initial accretion disc. Taking a look at the observations they seem to indicate the process to take 6 days, at which time the SSS starts and the gradient of the light curve steepens, in accordance to a change in the optical and UV source.

The physical process can be modelled simply by assuming that after the eruption we start reformation of the accretion disc with a messy atmosphere filling the Roche lobe around the WD. Whether this atmosphere consists of large blobs moving under gravity nearly like solid bodies or is fully turbulent, the momentum in vertical motions will dissipate with each crossing of the orbital plane, since atmospheric elements with opposite momentum will interact. We can identify the spectral signature of this turbulent material with the UV-optical spectral energy distribution (SED). The variable line components seen in He II are taken as an indication of the blob velocities of order 3000 km s⁻¹ (the He II FWZI is 10 000 km s⁻¹). With the disc formation and clearing out of the WD Roche lobe within 6 d the disc is not necessarily stationary, since the mass inflow may still evolve either from the secondary or from enhanced inflow from the heated atmosphere of the secondary. Since orbits closer to the WD mean higher velocities, dissipation of energy and relaxation times will, similarly to an accretion disc, be larger near the WD. This scenario provides an update to the simple picture of the formation of an accretion disc by Verbunt (1982) for novae.

5.4 H burned to He during the SSS-phase

During the SSS phase steady nuclear burning takes place on the surface of the WD. The burning is eventually quenched due to a drop in the temperature and pressure, which in turn happens when the hydrogen that fuels the luminosity runs low. We can assume that the steady burning occurred from the time of the explosive ejection of material until the time of turn-off. The SSS luminosity is thus a way to measure how much He is added to the WD during that period, regardless of the source of the H being pre- or post-eruption. The difference between He ejected and added due to burning during the SSS phase gives an indication of the rate of growth of the WD mass.

A blackbody fit to the X-ray spectrum shows that during the SSS phase the luminosity of the surface is 1.1×10^{37} erg s⁻¹ (Section 5.6, Fig. 9). The downturn in the light curve starts at day 30, so in 30 d

the energy produced was 2.8×10^{43} erg. Assuming one gram of H converted to ⁴He produces 6.40×10^{18} erg, the total He mass created is $M(\text{He}) = 4.4 \times 10^{24}$ g = $2.2 \times 10^{-9} M_{\odot}$. If the accreting matter were high in He, the estimated growth in WD mass is a lower limit.

In N LMC 1968 the He abundance is very high (Shore et al. 1991). This may be due to He-rich ejecta or because the secondary has lost most of its hydrogen. In our proposed messy atmosphere the variable He II line component would be in the inner Roche lobe in the early days after the eruption but it is unclear how it got there.

5.5 Estimate of the ejected mass

The quiescent luminosity is thought to be dominated by the accretion disc luminosity L_{acc} . Taking the photometry from around day 70 we can construct an SED (1900–9000 Å). We estimate $L_{\text{acc}} \geq 4 \times 10^{34}$ ergs⁻¹ where the lower limit is because the dereddened spectrum has an unaccounted component which is still rising in the UV. This translates to an accreted mass of at least $M_{\text{acc}} \geq 3.5 \times 10^{-8} M_{\odot}$ using Osborne et al. (2011).

Under an assumption that the bipolar ejecta cross our line of sight, and there is no debris left in the inner Roche lobes, we can use the start time of the SSS phase to derive an estimate of the ejected mass along the line of sight, since that happens when the N_{H} column reaches a value where the soft X-rays become transparent while we also know at what time the SSS rise occurs. Multiplying that time with the measured ejecta velocity then gives the distance to use with N_{H} . On day 7.2, $N_{\text{H}} = 4 \times 10^{21}$ cm⁻², while $V_{\text{ej}} = 5000$ km s⁻¹. Of course, for extrapolating that to the total ejected mass we will have to make some estimate of the geometry of the ejecta. Since the ejecta are bipolar, the ejecta covers a solid angle Ω , and we derive an ejecta mass of $\approx 3 \times 10^{-7} (\Omega/(4\pi)) M_{\odot}$. Assuming the accreted mass is 2–3 times the lower limit above and a solid angle of $\approx \pi$, the numbers for accreted and ejected mass are compatible with $M_{\text{ej}} \approx 10^{-7} M_{\odot}$, but do not allow a determination of net mass-loss or growth for the WD.

5.6 The UV and X-ray luminosities

The peak UV luminosity (1200–3300 Å) of N LMC 1968 in the 1990 outburst was computed by Shore et al. (1991) to exceed the Eddington luminosity (1.6×10^{38} erg s⁻¹ for a 1.3 M_{\odot} WD), but with our adopted smaller distance, reddening and N_{H} , the luminosity is nearly a factor 4 smaller: Using the SED derived from the normalization of the light curve fit at day 1.0 (see Section 3) and fitting that with a blackbody, the peak luminosity of the UV-optical component is $L_{\text{UV}} \approx 4 \times 10^{37}$ erg s⁻¹. We also tried to fit the dereddened continuum of the combined day 2 to 4 spectra using the 1990 *IUE* as well as the 2016 day 2.9 UVOT and day 3.95 IMACS spectra, covering 1150–9000 Å, but a single blackbody fit is not possible. The UV rise suggests a temperature in excess of ~ 25 000 K plus a cool component to deal with excess IR flux.

After the initial ejection, the WD luminosity becomes thermalized by the optically thick ejecta, but once the ejecta have become optically thin, the luminosity comes out in the X-ray and EUV. We found in Section 3.11 that $L_{\text{X-Bol}} \approx 1.1 \times 10^{37}$ erg s⁻¹. The UV-optical light during the SSS is by then much less than near the peak: A blackbody fit for the UV-optical component at that time gives $L_{\text{UV}} = 2.4 \times 10^{35}$ erg s⁻¹.

A review of the past eruptions suggest the rise time to peak is about a day. Using the estimate for the ejected mass and the

Table 3. Summary of the parameters for N LMC 1968.

Property	Value	Unit	Section
2016 eruption JD	2457 408.709 ± 0.8		2.5
Adopted distance LMC	50	kpc	2.1
Minimum mag $\langle V_{min} \rangle$	19.70	mag	
Maximum mag V_{max}	12.3 ± 0.5	mag	
Decay time 2 mag t_2	4.6 ± 0.5	d	3.7
Decay time 3 mag t_3	7 ± 1	d	3.7
Epoch binary	2455058.323 ± 0.090	HJD	3.8
Period	1.26433 ± 0.000019	d	3.8
Period change $\Delta P/P$	< 0.003		3.8
Reddening $E(B - V)$	0.07	mag	4.3
Interstellar N_H	1.8×10^{21}	cm^{-2}	3.11
SSS emission phase	6–57	d	3.2
SSS typical luminosity	1.1×10^{37}	erg/s	3.11
Kinetic energy	$\approx 10^{38}$	erg/s	5.6
SSS typical BB temp.(kT)	100	eV	3.11
Narrow component FWZI	1.6×10^3	$km s^{-1}$	3.9
FWZI broad component	10^4	$km s^{-1}$	3.9
Sp. type secondary	Unknown		4.1
Ejecta velocity	5000	$km s^{-1}$	3.9
WD mass	> 1.3	M_{\odot}	4.2
Depth eclipse	0.6	mag	3.8
Duration eclipse	0.05	phase	3.8
Ejected mass	$\approx 10^{-7}$	M_{\odot}	5.5
H converted to ${}^4\text{He}$	2.2×10^{-9}	M_{\odot}	5.4
System inclination	68–76	degrees	5.2
Recurrence time	6.2 ± 1.2	yr	2.6
UV–optical $L(1 \text{ d})$	4×10^{37}	$erg s^{-1}$	5.6
Peak $L_X(14\text{--}30 \text{ d})$	1.1×10^{37}	$erg s^{-1}$	5.6

expansion velocity, the kinetic energy rate imparted in the first day is around $3 \times (\Omega/4\pi) \times 10^{38} \text{ erg s}^{-1}$, with Ω the solid angle of the ejecta. This suggests that the kinetic energy imparted the first day of the eruption is close to the Eddington luminosity, and dominates over the energy lost in radiation.

6 CONCLUSIONS

In Table 3 the main parameters which have been derived are collected.

The recurrence time of N LMC 1968 is short and we expect another explosion to happen around April 2022 ± 1.2 yr. In this study we collected and interpreted the known data from which we derived the ephemeris for the WD eclipse. Though the system shows eclipses, we do not have radial velocity measurements which would help determine the orbit and mass ratio of the binary.

The radiant luminosity is found to be lower than Eddington for a He-atmosphere by an order of magnitude, unlike in many other novae. If the intrinsic luminosity of the nova is near Eddington, the lower observed value could be due to shadowing by the accretion disc, where only Thompson scattering of the X-rays in a halo above the orbital plane of the system is observed. However, the kinetic energy in the ejecta required an Eddington luminosity during the initial TNR. This could mean that for the rapid recurrent systems the kinetic energy dominates over the observed radiative component.

We also observe evidence that suggests that prior to day 7 (after the eruption) there is a source of gravitationally bound material in the system, possibly due to increased mass flow from the secondary, disruption of the accretion disc, or part of the WD atmosphere

that did not reach escape speed. This is seen as a variable He⁺-rich matter component which shows orbital periodicity day 2–7 after the 1990 eruption and could be located in the inner Roche lobe or just outside it. The eventual collapse of this matter into the orbital plane could bring about the emergence of the WD soft X-ray emission. The rise of the SSS emission could alternatively be due to the decreasing column density in the expanding bipolar ejecta.

A sudden increase in the Fe II UV absorption on day 4 is seen as evidence for a reionization wave happening in the ejecta.

Linking the SSS luminosity to steady burning on the WD surface we arrive at an estimate of the mass of H converted to He after the eruption. This matter is adding to the WD mass, providing a link between SSS duration and growth of the WD. We also estimate the ejected mass and find that to be compatible with the accretion rate. The high SSS temperature suggests the WD mass is larger than $1.3 M_{\odot}$.

In the UV we observe eclipses out to 320 d after the 2016 eruption which are shallow and broad while the emission is variable, suggesting that the accretion disc is not stable or is perhaps warped.

The current study has left many questions. Some of those could be answered by future high-resolution multispectral observations of the different phases of the eruption, and better characterization of the orbital parameters. A comparison of the very similar Galactic nova U Sco to N LMC 1968, which has a similar orbital period $P_{\text{orb}} = 1.2305 \text{ d}$ (Schaefer et al. 2011) and recurrence time of $10 \pm 2 \text{ yr}$ (Schaefer 2010) is planned for future work.

ACKNOWLEDGEMENTS

The OGLE project received funding by the National Science Center, Poland, under grant MAESTRO 2014/14/A/ST9/00121 to AU. PM acknowledges support from the Foundation for Polish Science (Program START). NPMK, KLP, AAB, APB, and JPO acknowledge support from the U.K. Space Agency. MH acknowledges the support of the Spanish Ministry of Economy and Competitiveness (MINECO) under the grant FDPI-2013-16933. SS acknowledges partial support from NASA, *HST*, and NSF grants to ASU. Research in Novae at Stony Brook University is supported in part by NSF grant AST 1614113, with additional research support provided by the Stony Brook University. RDG was supported by NASA and the United States Air Force. VARMR acknowledges financial support from the Fundação para a Ciência e a Tecnologia (FCT) in the form of an exploratory project of reference IF/00498/2015, from the Center for Research & Development in Mathematics and Applications (CIDMA) strategic project UID/MAT/04106/2019, and supported by Enabling Green E-science for the Square Kilometre Array Research Infrastructure (ENGAGE-SKA), POCI-01-0145-FEDER-022217, and PHOBOS, POCI-01-0145-FEDER-029932, funded by Programa Operacional Competitividade e Internacionalização (COMPETE 2020) and FCT, Portugal. RA acknowledges financial support from DIDULS Regular PR#17142 by Universidad de La Serena. The Swift data were retrieved from the UK Swift Data centre. *IUE* spectra were retrieved from the MAST archive. This work makes use of observations from the Las Cumbres Observatory network. We acknowledge with thanks the variable star observations from the AAVSO International Database contributed by observers worldwide and used in this research. We would like to acknowledge Elena Mason, and Bob Williams for discussions, Mike Shara, Kaz Sekiguchi, and David Buckley who tried to chase down old observations of

this nova, and Patrick Godon for discussions on the accretion disc. We used HEASARC FTOOLS, IDL, SCIPY, MATPLOTLIB, and ASTROPY.

REFERENCES

- Alcock C. et al., 1992, in Filippenko A. V., ed., ASP Conf. Ser. Vol. 103, Robotic Telescopes in the 1990s. Astron. Soc. Pac., San Francisco, p. 193
- Alcock C. et al., 1999, *PASP*, 111, 1539
- Alcock C. et al., 2000, *ApJ*, 542, 281
- Anupama G. C. et al., 2013, *A&A*, 559, A121
- Aydi E. et al., 2018, *MNRAS*, 474, 2679
- Bhardwaj A., Macri L. M., Rejkuba M., Kanbur S. M., Ngeow C.-C., Singh H. P., 2017, *AJ*, 153, 154
- Bode M. F., Evans A., 2008, Cambridge Astrophysics Series, No. 43, Classical Novae, Cambridge University Press, Cambridge
- Bode M. F. et al., 2016, *ApJ*, 818, 145
- Bohlin R. C., Savage B. D., Drake J. F., 1978, *ApJ*, 224, 132
- Bond H. E., Walter F., Espinoza J., Gonzalez D., Pasten A., Green D. W. E., 2004, IAU Circ., 8424, 1
- Börngen F., 1968, *Astron. Nachr.*, 291, 19
- Breeveld A. A., Landsman W., Holland S. T., Roming P., Kuin N. P. M., Page M. J., 2011, in McEnery J. E., Racusin J. L., Gehrels N., eds, Proc. AIP Conf. Ser. Vol. 1358, Gamma Ray Bursts 2010, Am. Inst. Phys., New York, p. 373
- Burrows D. N. et al., 2005, *Space Sci. Rev.*, 120, 165
- Cardelli J. A., Clayton G. C., Mathis J. S., 1989, *ApJ*, 345, 245
- Carvalho G. A., Marinho R. M., Malheiro M., 2018, *Gen. Relativ. Gravit.*, 50, 38
- Casanova J., José J., García-Berro E., Shore S. N., 2016, *A&A*, 595, A28
- Cash W., 1979, *ApJ*, 228, 939
- Chandrasekhar S., 1931, *ApJ*, 74, 81
- Chen H.-L., Woods T. E., Yungelson L. R., Gilfanov M., Han Z., 2016, *MNRAS*, 458, 2916
- Darnley M., Henze M., 2018, in 42nd COSPAR Scientific Assembly, COSPAR, Pasadena, California., p. E1.7–36-18
- Darnley M. J., Henze M., 2019, preprint ([arXiv:1909.10497](https://arxiv.org/abs/1909.10497))
- Darnley M. J. et al., 2006, *MNRAS*, 369, 257
- Darnley M. J., Ribeiro V. A. R. M., Bode M. F., Hounsell R. A., Williams R. P., 2012, *ApJ*, 746, 61
- Darnley M. J., Williams S. C., Bode M. F., Henze M., Ness J. U., Shafter A. W., Hornoch K., Votruba V., 2014, *A&A*, 563, L9
- Darnley M. J. et al., 2015, *A&A*, 580, A45
- Darnley M. J. et al., 2016a, *ApJ*, 833, 149
- Darnley M. J., Kuin N. P. M., Page K. L., Osborne J. P., Schwarz G. J., Shore S. N., Starrfield S., Williams S. C., 2016b, *Astron. Telegram*, 8587, 1
- Darnley M. J. et al., 2019, *Nature*, 565, 460
- Di Mille F., Angeloni R., Morrell N., 2016, *Astron. Telegram*, 8586, 1
- Drake J. J., Orlando S., 2010, *ApJ*, 720, L195
- Duerbeck H. W., 1988, *A&A*, 197, 148
- Evans A., Bode M. F., O'Brien T. J., Darnley M. J., Eds. 2008, ASP Conf. Ser. Vol. 401, RS Ophiuchi (2006) and the Recurrent Nova Phenomenon. Astron. Soc. Pac., San Francisco
- Figueira J., José J., García-Berro E., Campbell S. W., García-Senz D., Mohamed S., 2018, *A&A*, 613, A8
- Fitzpatrick E. L., 1986, *AJ*, 92, 1068
- Fragner M. M., Nelson R. P., 2010, *A&A*, 511, A77
- Gaposchkin C. H. P., 1957, *The Galactic Novae*, Dover, New York
- Gehrels N. et al., 2004, *ApJ*, 611, 1005
- Gill C. D., O'Brien T. J., 1999, *MNRAS*, 307, 677
- Gill C. D., O'Brien T. J., 2000, *MNRAS*, 314, 175
- Girardi L., 2016, *ARA&A*, 54, 95
- Gutierrez J., Garcia-Berro E., Iben Icko J., Isern J., Labay J., Canal R., 1996, *ApJ*, 459, 701
- Harman D. J., O'Brien T. J., 2003, *MNRAS*, 344, 1219
- Henden A. A., Levine S. E., Terrell D., Smith T. C., Welch D., 2012, *J. Am. Assoc. Var. Star Obs.*, 40, 430
- Henze M., Meusinger H., Pietsch W., 2008, *A&A*, 477, 67
- Henze M. et al., 2014a, *A&A*, 563, A2
- Henze M., Ness J. U., Darnley M. J., Bode M. F., Williams S. C., Shafter A. W., Kato M., Hachisu I., 2014b, *A&A*, 563, L8
- Henze M. et al., 2015, *A&A*, 580, A46
- Henze M. et al., 2018, *ApJ*, 857, 68
- Hernanz M., José J., 2008, *New Astron. Rev.*, 52, 386
- Hillebrandt W., Niemeyer J. C., 2000, *ARA&A*, 38, 191
- Hillman Y., Prialnik D., Kovetz A., Shara M. M., 2016, *ApJ*, 819, 168
- Hubble E. P., 1929, *ApJ*, 69, 103
- Hutchings J. B., 1972, *MNRAS*, 158, 177
- Kafka S., Williams R., 2011, *A&A*, 526, A83
- Kalberla P. M. W., Burton W. B., Hartmann D., Arnal E. M., Bajaja E., Morras R., Pöppel W. G. L., 2005, *A&A*, 440, 775
- Koornneef J., 1982, *A&A*, 107, 247
- Krautter J., Oegelman H., Starrfield S., Wichmann R., Pfeffermann E., 1996, *ApJ*, 456, 788
- Kuin P., 2014, Astrophysics Source Code Library, record [ascl:1410.004](https://www.ascl.net/asn/ascl:1410.004)
- Kuin N. P. M. et al., 2015, *MNRAS*, 449, 2514
- Landolt A. U., 2009, *AJ*, 137, 4186
- Liller W., 1990, IAU Circ., 4961, 2
- Liller W., Herald D., McNaught R. H., Pearce A., Seargent D. A. J., 1987, IAU Circ., 4428, 1
- Liller W., Shida R. Y., Jones A. F., 2004, *Inf. Bull. Var. Stars*, 5582, 1
- Liszt H., 2014, *ApJ*, 780, 10
- Livio M., Mazzali P., 2018, *Phys. Rep.*, 736, 1
- Luyten W. J., 1927, *Harv. Coll. Obs. Bull.*, 847, 8
- Markwardt C. B., 2009, in Bohlender D. A., Durand D., Dowler P., eds, ASP Conf. Ser. Vol. 411, Astronomical Data Analysis Software and Systems XVIII. Astron. Soc. Pac., San Francisco, p. 251
- Mason K. O., Breeveld A., Hunsberger S. D., James C., Kennedy T. E., Roming P. W. A., Stock J., 2004a, in Flanagan K. A., Siegmund O. H. W., eds, Proc. SPIE Conf. Ser. Vol. 5165, X-Ray and Gamma-Ray Instrumentation for Astronomy XIII. SPIE, Bellingham, p. 277
- Mason E., Ederoclite A., Stefanon M., dall T. H., Della Valle M., 2004b, IAU Circ., 8424, 2
- Mason E., Ederoclite A., Williams R. E., Della Valle M., Setiawan J., 2012, *A&A*, 544, A149
- Mroz P., Udalski A., 2016, *Astron. Telegram*, 8578, 1
- Mroz P., Udalski A., 2018, *Astron. Telegram*, 11384, 1
- Mróz P. et al., 2014, *MNRAS*, 443, 784
- Mróz P. et al., 2016, *ApJS*, 222, 9
- Munari U., Moretti S., 2012, *Balt. Astron.*, 21, 22
- Munari U., Valisa P., 2014, *Contrib. Astron. Obs. Skalnaté Pleso*, 43, 174
- Munari U. et al., 2012, *Balt. Astron.*, 21, 13
- Munari U., Henden A., Frigo A., Dallaporta S., 2014a, *J. Astron. Data*, 20, 4
- Munari U. et al., 2014b, *AJ*, 148, 81
- Munari U., Walter F. M., Hamsch F.-J., Frigo A., 2016, *Inf. Bull. Var. Stars*, 6162, 1
- Mustel E. R., Boyarchuk A. A., 1970, *Ap&SS*, 6, 183
- Ness J. U. et al., 2009, *AJ*, 137, 4160
- Ness J. U. et al., 2013, *A&A*, 559, A50
- Nichols J. S., Linsky J. L., 1996, *AJ*, 111, 517
- Orio M. et al., 2013, *MNRAS*, 429, 1342
- Osborne J. P., 2015, *J. High Energy Astrophys.*, 7, 117
- Osborne J. P. et al., 2011, *ApJ*, 727, 124
- Page K. L., Osborne J. P., Wagner R. M., Beardmore A. P., Shore S. N., Starrfield S., Woodward C. E., 2013, *ApJ*, 768, L26
- Page K. L. et al., 2015a, *MNRAS*, 454, 3108
- Page K. L. et al., 2015b, *MNRAS*, 454, 3108
- Pagnotta A., Schaefer B. E., 2014, *ApJ*, 788, 164

- Pagnotta A., Schaefer B. E., Xiao L., Collazzi A. C., Kroll P., 2009, *AJ*, 138, 1230
- Pagnotta A. et al., 2015, *ApJ*, 811, 32
- Pietrzyński G. et al., 2013, *Nature*, 495, 76
- Pietrzyński G. et al., 2019, *Nature*, 567, 200
- Pietsch W., 2010, *Astron. Nachr.*, 331, 187
- Pietsch W. et al., 2007, *A&A*, 465, 375
- Pojmanski G., 2002, *Acta Astron.*, 52, 397
- Prialnik D., Kovetz A., 1995, *ApJ*, 445, 789
- Ribeiro V. A. R. M. et al., 2009, *ApJ*, 703, 1955
- Ribeiro V. A. R. M., Bode M. F., Darnley M. J., Barnsley R. M., Munari U., Harman D. J., 2013a, *MNRAS*, 433, 1991
- Ribeiro V. A. R. M., Munari U., Valisa P., 2013b, *ApJ*, 768, 49
- Roming P. W. A. et al., 2005, *Space Sci. Rev.*, 120, 95
- Rosino L., 1964, *Ann. Astrophys.*, 27, 498
- Sala G., Hernanz M., 2005, *A&A*, 439, 1061
- Schaefer B. E., 2010, *ApJS*, 187, 275
- Schaefer B. E., Ringwald F. A., 1995, *ApJ*, 447, L45
- Schaefer B. E. et al., 2011, *ApJ*, 742, 113
- Schwarzenberg-Czerny A., 1996, *ApJ*, 460, L107
- Schwarz G. J. et al., 2011, *ApJS*, 197, 31
- Sekiguchi K., Feast M. W., Whitelock P. A., Overbeek M. D., Wargau W., Jones J. S., 1988, *MNRAS*, 234, 281
- Sekiguchi K. et al., 1989, *MNRAS*, 236, 611
- Sekiguchi K., Stobie R. S., Buckley D. A. H., Caldwell J. A. R., 1990, *MNRAS*, 245, 28P
- Shafter A. W., 2013, *AJ*, 145, 117
- Shafter A. W., 2017, *ApJ*, 834, 196
- Shafter A. W. et al., 2015, *ApJS*, 216, 34
- Shara M. M. et al., 2016, *ApJS*, 227, 1
- Shore S. N., 2012, *Bull. Astron. Soc. India*, 40, 185
- Shore S. N., Sonneborn G., Starrfield S. G., Hamuy M., Williams R. E., Cassatella A., Drechsel H., 1991, *ApJ*, 370, 193
- Shore S. N., Starrfield S., Sonneborn G., 1996, *ApJ*, 463, L21
- Shore S. N., Schwarz G. J., De Gennaro Aquino I., Augusteijn T., Walter F. M., Starrfield S., Sion E. M., 2013a, *A&A*, 549, A140
- Shore S. N., De Gennaro Aquino I., Schwarz G. J., Augusteijn T., Cheung C. C., Walter F. M., Starrfield S., 2013b, *A&A*, 553, A123
- Shore S. N. et al., 2016, *A&A*, 590, A123
- Shore S. N., Kuin N. P., Mason E., De Gennaro Aquino I., 2018, *A&A*, 619, A104
- Sievers J., 1970, *Inf. Bull. Var. Stars*, 448, 1
- Smith J. A. et al., 2002, *AJ*, 123, 2121
- Solf J., 1983, *ApJ*, 273, 647
- Soraisam M. D., Gilfanov M., Wolf W. M., Bildsten L., 2016, *MNRAS*, 455, 668
- Starrfield S. et al., 1988a, in *ESA Special Publication. Vol. 281*, ESA, Noordwijk, The Netherlands, p. 167
- Starrfield S., Sparks W. M., Shaviv G., 1988b, *ApJ*, 325, L35
- Starrfield S., Iliadis C., Timmes F. X., Hix W. R., Arnett W. D., Meakin C., Sparks W. M., 2012, *Bull. Astron. Soc. India*, 40, 419
- Starrfield S., Iliadis C., Hix W. R., 2016, *PASP*, 128, 051001
- Tang S. et al., 2014, *ApJ*, 786, 61
- Tisserand P. et al., 2007, *A&A*, 469, 387
- Udalski A., Szymanski M. K., Soszynski I., Poleski R., 2008, *Acta Astron.*, 58, 69
- Udalski A., Szymański M. K., Szymański G., 2015, *Acta Astron.*, 65, 1
- Verbunt F., 1982, *Space Sci. Rev.*, 32, 379
- Verbunt F., 1987, *A&AS*, 71, 339
- Walter F. M., Battisti A., Towers S. E., Bond H. E., Stringfellow G. S., 2012, *PASP*, 124, 1057
- Whelan J., Iben Icko J., 1973, *ApJ*, 186, 1007
- Williams R. E., Sparks W. M., Gallagher J. S., Ney E. P., Starrfield S. G., Truran J. W., 1981, *ApJ*, 251, 221
- Williams R. E., Hamuy M., Phillips M. M., Heathcote S. R., Wells L., Navarrete M., Duerbeck H. W., 2003, *J. Astron. Data*, 9, 3
- Williams S. C., Darnley M. J., Bode M. F., Shafter A. W., 2016, *ApJ*, 817, 143
- Wolf W. M., Bildsten L., Brooks J., Paxton B., 2013, *ApJ*, 777, 136
- Woudt P. A., Ribeiro V. A. R. M., eds., 2014, *ASP Conf. Ser. Vol. 490*, *Stella Novae: Past and Future Decades*. Astron. Soc. Pac., San Francisco
- Yaron O., Prialnik D., Shara M. M., Kovetz A., 2005, *ApJ*, 623, 398

APPENDIX A

Table A1. All known UV-optical spectra of N LMC 1968 ordered by day since respective outburst.

Mission or instrument ^a	Year eruption	Midtime JD (d)	Day since eruption	Orbital phase ^b (2)	ID and notes
CTIO/Argus	1990	2447 936.6	0.0	0.19	Discovery spectrum ^c
<i>IUE</i>	1990	2447 938.511 49	1.92	0.70	SWP38199
<i>IUE</i>	1990	2447 938.551 07	1.95	0.73	LWP17374
<i>IUE</i>	1990	2447 938.564 80	1.97	0.75	SWP38200
<i>IUE</i>	1990	2447 939.013 85	2.42	0.10	SWP38202
<i>IUE</i>	1990	2447 939.034 38	2.44	0.12	LWP17378
<i>IUE</i>	1990	2447 939.234 61	2.65	0.27	LWP17379
<i>IUE</i>	1990	2447 939.262 23	2.67	0.30	SWP38204
<i>IUE</i>	1990	2447 939.285 32	2.69	0.31	LWP17380
UVOT UVG	2016	2457 410.782 00	2.88	0.64	00045768005
UVOT UVG	2016	2457 411.329 73	3.43	0.07	00045768006
<i>IUE</i>	1990	2447 940.444 78	3.86	0.21–0.26	SWP38209
<i>IUE</i>	1990	2447 940.476 94	3.89	0.23–0.29	LWP17390
UVOT UVG	2016	2457 411.777 83	3.88	0.4260	00045768007
LCO IMACS	2016	2457 411.5351	3.945	0.23	Fits file
UVOT UVG	2016	2457 411.911 22	4.01	0.5315	00045768008
UVOT UVG	2016	2457 412.975 19	5.07	0.3730	00045768009
UVOT UVG	2016	2457 413.121 85	5.22	0.4890	00045768010

Table A1 – *continued*

Mission or instrument ^a	Year eruption	Midtime JD (d)	Day since eruption	Orbital phase ^b (2)	ID and notes
<i>IUE</i>	1990	2447 942.344 66	5.77	0.68–0.79	SWP38214
UVOT UVG	2016	2457 414.047 20	6.14	0.2209	00034302002
UVOT UVG	2016	2457 415.112 69	7.21	0.0636	00034302004
SAAO	1990	2447 944.31	7.71	0.29	Not recoverable
Mirranook Armidale	2016	2457 415.9501	8.05	0.73	Fits file
UVOT UVG	2016	2457 416.039 41	8.13	0.7966	00034302006
SAAO	1990	2447 945.33	8.73	0.10	Published
UVOT UVG	2016	2457 416.706 04	8.80	0.3239	00034302008
<i>IUE</i>	1990	2447 945.504 90	8.93	0.71–0.82	SWP38229
CTIO	1990	2447 945.6029	9.00	0.31	Fits file
FTS/FLOYDS	2016	2457 417.1	9.2	0.63	Fits file
<i>IUE</i>	1990	2447 946.251 25	9.69	0.74–0.91	SWP38231
UVOT VG	2016	2457 417.636 02	9.73	0.5940	00034302010
UVOT VG	2016	2457 418.036 03	10.13	0.3758	00034302012
SAAO	1990	2447 948.29	11.69	0.44	Not recoverable
SAAO	1990	2447 952.36	15.76	0.66	Published
<i>IUE</i>	1990	2447 952.884 44	16.35	0.95–0.20	SWP38284
LCO duPont	2016	2457 427.6486	19.73	0.98	Fits file
LCO duPont	2016	2457 428.6344	20.72	0.76	Fits file
LCO duPont	2016	2457 429.5827	21.67	0.51	Fits file
<i>IUE</i>	1990	2447 970.873 19	34.35	0.15–0.45	SWP38394
<i>IUE</i>	1990	2447 976.810 65	40.35	0.72–0.27	SWP38439
<i>IUE</i>	1990	2447 977.811 34	41.35	0.73–0.28	LWP17625
LCO IMACS	2016	2457 476.5447	68.64	0.65	Fits file
LCO IMACS	2016	2457 476.5690	68.67	0.67	Fits file

^aSpectral ranges per instrument: *IUE* SWP is 1150–2000Å; *IUE* LWP is 1800–3300Å, UVOT UVGRISM is 1700–5000Å; UVOT VGRISM is 2900–6600Å; CTIO is 3500–7700Å; Magellan/IMACS is 4000–9000Å; SAAO is 3500–7200Å; FTS/Floyds 3300–11000Å.

^bFor the 1990 eruption the orbital phase uncertainty is 0.15 and based on equation (2). The range in phase is due to long observations, e.g. for *IUE*, otherwise ≤ 0.02 .

^cThis has been lost, unfortunately. Personal communication with Mike Shara and Bob Williams.

Table A2. Swift UVOT Grism exposures.

Mid-time ^a JD(+2450000)	Day ^b	Orbital ^a phase	Swift OBSID	Roll deg	Anchor ^c (X, Y)pix	Exposure time (s)	UV/V grism	<i>uvw1</i> ^d	Scale ^e factor
7410.782 00	2.88	0.6383	00045768005	219.1	1046, 875	285.3	UV	13.642	1.00
7411.329 73	3.43	0.0716	00045768006	223.0	1235, 925	405.0	UV	13.723	1.08
7411.777 83	3.88	0.4260	00045768007	216.0	1198, 1034	282.3	UV	13.697	1.05
7411.911 22	4.01	0.5315	00045768008	220.0	1263, 945	285.9	UV	13.694	1.05
7412.975 19	5.07	0.3730	00045768009	217.0	1270, 834	294.3	UV	14.363	1.95
7413.121 85	5.22	0.4890	00045768010	221.1	1106, 886	398.8	UV	14.624	2.48
7414.047 20	6.14	0.2209	00034302002	237.0	1130, 1613	892.5	UV	15.614	6.16
7415.112 69	7.21	0.0636	00034302004	222.0	972, 1620	946.6	UV	15.822	7.46
7416.039 41	8.13	0.7966	00034302006	223.0	1034, 1590	999.7	UV	15.884	7.90
7416.706 04	8.80	0.3239	00034302008	223.0	952, 1636	892.5	UV	16.156	10.15
7417.636 02	9.73	0.5940	00034302010	232.0	1114, 1662	892.5	V	16.586	15.08
7418.036 03	10.13	0.3758	00034302012	232.0	1101, 1638	892.5	V	16.675	16.37

^aMid-time of exposure.

^bDays since estimated time of eruption JD 2457 407.9.

^cThe anchor is defined by the position in the first order spectrum at 260 nm (UV) or 420 nm (V).

^d*uvw1* magnitude interpolated from a spline fit to the light curve.

^eFlux scale factor derived from *uvw1* light curve.

Table A3. Photometry from 10 d before to 50 d after the 2016 eruption of N LMC 1968.^a

Date ^a (MJD)	mag	mag error	Orbital ^c phase	Instrument and filter	phot. system
7399.24670	19.297	0.042	0.910 14	OGLE I	Vega
7404.23630	19.422	0.042	0.856 58	OGLE I	Vega
7408.20942	99.999	9.999	0.999 06	OGLE I	Vega
7410.04082	12.820	0.005	0.447 58	Andicam I	Vega
7410.04157	13.298	0.004	0.448 17	Andicam B	Vega
7410.05324	13.556	0.008	0.457 40	Andicam V	Vega
7410.05391	12.605	0.005	0.457 93	Andicam R	Vega
7410.17573	12.774	0.056	0.554 28	ANS	Vega
7410.17573	13.211	0.032	0.554 28	ANS	Vega
7410.17573	13.228	0.028	0.554 28	ANS	Vega
7410.21081	12.930	0.003	0.582 02	OGLE I	Vega
7410.27711	13.643	0.023	0.634 46	UVOT UVW1	AB
7410.82572	13.710	0.027	0.068 38	UVOT UVW1	AB
7411.17503	13.110	0.029	0.344 66	ANS	Vega
7411.17503	13.573	0.013	0.344 66	ANS	Vega
7411.17503	13.628	0.022	0.344 66	ANS	Vega
7411.27294	13.647	0.023	0.422 10	UVOT UVW1	AB
7411.40628	13.793	0.024	0.527 56	UVOT UVW1	AB
7412.06793	13.868	0.012	0.050 88	Andicam I	Vega
7412.06864	14.110	0.007	0.051 45	Andicam B	Vega
7412.06939	14.316	0.016	0.052 04	Andicam V	Vega
7412.07005	13.825	0.011	0.052 56	Andicam R	Vega
7412.08291	13.768	0.003	0.062 73	OGLE I	Vega
7412.17229	13.808	0.040	0.133 42	ANS	Vega
7412.17229	14.030	0.023	0.133 42	ANS	Vega
7412.17229	14.117	0.019	0.133 42	ANS	Vega
7412.24426	13.774	0.012	0.190 35	Andicam I	Vega
7412.25706	14.180	0.015	0.200 47	Andicam V	Vega
7412.25797	13.620	0.012	0.201 19	Andicam R	Vega
7412.47017	14.052	0.024	0.369 02	UVOT UVW1	AB
7412.61739	14.902	0.031	0.485 47	UVOT UVW1	AB
7413.16938	14.257	0.058	0.922 06	ANS	Vega
7413.16938	14.531	0.034	0.922 06	ANS	Vega
7413.16938	14.597	0.030	0.922 06	ANS	Vega
7413.17357	14.234	0.003	0.925 37	OGLE I	Vega
7413.53753	14.515	0.024	0.213 23	UVOT UVW2	AB
7413.55142	14.574	0.030	0.224 22	UVOT UVW2	AB
7414.13745	14.791	0.048	0.687 74	Andicam I	Vega
7414.14558	15.311	0.013	0.694 17	Andicam B	Vega
7414.14966	14.998	0.009	0.697 39	Andicam V	Vega
7414.15374	14.715	0.014	0.700 62	Andicam R	Vega
7414.16670	14.390	0.072	0.710 87	ANS	Vega
7414.16670	14.586	0.028	0.710 87	ANS	Vega
7414.16670	14.839	0.071	0.710 87	ANS	Vega
7414.26437	14.501	0.003	0.788 12	OGLE I	Vega
7414.60489	15.596	0.039	0.057 45	UVOT UVM2	AB
7414.61739	15.732	0.036	0.067 33	UVOT UVW2	AB
7415.15130	15.604	0.008	0.489 62	Andicam I	Vega
7415.15305	15.983	0.006	0.491 01	Andicam B	Vega
7415.15484	16.013	0.010	0.492 42	Andicam V	Vega
7415.15605	15.573	0.008	0.493 38	Andicam R	Vega
7415.16300	15.396	0.003	0.498 88	OGLE I	Vega
7415.52989	15.873	0.031	0.789 06	UVOT UVW1	AB
7415.54447	16.009	0.039	0.800 59	UVOT UVW2	AB
7416.15497	16.253	0.014	0.283 46	Andicam I	Vega
7416.15677	16.565	0.008	0.284 88	Andicam B	Vega
7416.15852	16.591	0.014	0.286 27	Andicam V	Vega
7416.15977	16.193	0.013	0.287 26	Andicam R	Vega
7416.16446	15.929	0.132	0.290 96	ANS	Vega
7416.16446	16.228	0.054	0.290 96	ANS	Vega
7416.16446	16.260	0.071	0.290 96	ANS	Vega
7416.18044	16.216	0.004	0.303 60	OGLE I	Vega
7416.21044	16.167	0.064	0.327 33	UVOT UVW2	AB
7417.03829	16.251	0.043	0.982 11	ANS	Vega

Table A3 – *continued*

Date ^a (MJD)	mag	mag error	Orbital ^c phase	Instrument and filter	phot. system
7417.03829	16.780	0.019	0.982 11	ANS	Vega
7417.03829	17.075	0.028	0.98211	ANS	Vega
7417.13390	16.951	0.016	0.057 73	Andicam I	Vega
7417.13569	17.117	0.009	0.059 15	Andicam B	Vega
7417.13744	17.225	0.017	0.060 53	Andicam V	Vega
7417.13869	16.809	0.015	0.061 52	Andicam R	Vega
7417.14031	16.660	0.053	0.062 79	UVOT UVW1	AB
7417.52781	16.548	0.042	0.369 28	UVOT UVW1	AB
7417.54031	16.738	0.055	0.379 17	UVOT UVW1	AB
7418.08238	15.981	0.034	0.807 91	ANS	Vega
7418.08238	16.408	0.015	0.807 91	ANS	Vega
7418.08238	16.571	0.008	0.807 91	ANS	Vega
7418.12675	16.676	0.014	0.843 01	Andicam I	Vega
7418.12850	16.904	0.007	0.844 39	Andicam B	Vega
7418.13025	16.965	0.013	0.845 78	Andicam V	Vega
7418.13150	16.719	0.013	0.846 77	Andicam R	Vega
7418.45558	16.740	0.097	0.103 09	UVOT UVW1	AB
7419.10888	16.940	0.015	0.619 81	Andicam I	Vega
7419.11063	17.161	0.008	0.621 19	Andicam B	Vega
7419.11238	17.141	0.015	0.622 58	Andicam V	Vega
7419.11363	16.940	0.015	0.623 57	Andicam R	Vega
7419.15646	− 1.000	− 1.000	0.657 44	ANS	Vega
7419.15646	16.570	0.018	0.657 44	ANS	Vega
7419.15646	16.806	0.016	0.657 44	ANS	Vega
7420.04870	− 1.000	− 1.000	0.363 14	ANS	Vega
7420.04870	16.610	0.016	0.363 14	ANS	Vega
7420.04870	16.770	0.038	0.363 14	ANS	Vega
7420.11907	16.882	0.017	0.418 79	Andicam I	Vega
7420.12086	17.151	0.008	0.420 21	Andicam B	Vega
7420.12261	17.152	0.015	0.421 59	Andicam V	Vega
7420.12386	16.869	0.016	0.422 58	Andicam R	Vega
7420.25142	16.710	0.026	0.523 48	UVOT UVW1	AB
7420.65281	16.884	0.031	0.840 95	UVOT UVW1	AB
7421.03317	16.153	0.045	0.141 79	ANS	Vega
7421.03317	16.739	0.024	0.141 79	ANS	Vega
7421.03317	16.900	0.032	0.141 79	ANS	Vega
7421.15504	16.899	0.016	0.238 18	Andicam I	Vega
7421.15679	17.028	0.007	0.239 56	Andicam B	Vega
7421.15854	17.035	0.014	0.240 95	Andicam V	Vega
7421.15979	16.885	0.015	0.241 94	Andicam R	Vega
7421.51739	16.646	0.031	0.524 78	UVOT UVW1	AB
7421.58406	16.601	0.030	0.577 51	UVOT UVW1	AB
7422.04978	16.396	0.043	0.945 86	ANS	Vega
7422.04978	16.812	0.039	0.945 86	ANS	Vega
7422.04978	17.066	0.061	0.945 86	ANS	Vega
7422.09426	17.516	0.022	0.981 04	Andicam I	Vega
7422.09605	17.846	0.012	0.982 46	Andicam B	Vega
7422.09780	17.769	0.022	0.983 84	Andicam V	Vega
7422.09905	17.513	0.022	0.984 83	Andicam R	Vega
7423.18165	17.034	0.018	0.841 10	Andicam I	Vega
7423.18340	17.343	0.010	0.842 48	Andicam B	Vega
7423.18515	17.324	0.019	0.843 86	Andicam V	Vega
7423.18640	17.249	0.019	0.844 85	Andicam R	Vega
7424.04142	− 1.000	− 1.000	0.521 12	ANS	Vega
7424.04142	16.656	0.020	0.521 12	ANS	Vega
7424.04142	16.956	0.022	0.521 12	ANS	Vega
7424.11649	16.952	0.016	0.580 49	Andicam I	Vega
7424.11824	17.066	0.008	0.581 88	Andicam B	Vega
7424.11999	17.043	0.015	0.583 26	Andicam V	Vega
7424.12124	16.963	0.016	0.584 25	Andicam R	Vega
7424.12285	16.833	0.006	0.585 52	OGLE I	Vega
7425.12780	16.926	0.017	0.380 37	Andicam I	Vega
7425.12955	17.170	0.008	0.381 75	Andicam B	Vega
7425.13134	17.149	0.016	0.383 17	Andicam V	Vega

Table A3 – continued

Date ^a (MJD)	mag	mag error	Orbital ^c phase	Instrument and filter	phot. system
7425.13255	17.025	0.018	0.384 12	Andicam R	Vega
7425.16908	16.887	0.006	0.413 02	OGLE I	Vega
7426.15560	17.134	0.021	0.193 29	Andicam I	Vega
7426.15735	17.224	0.009	0.194 67	Andicam B	Vega
7426.15914	17.192	0.017	0.196 09	Andicam V	Vega
7426.16035	17.093	0.019	0.197 05	Andicam R	Vega
7426.16622	16.974	0.008	0.201 69	OGLE I	Vega
7427.14781	17.542	0.009	0.978 06	OGLE I	Vega
7428.10171	17.178	0.018	0.732 54	Andicam I	Vega
7428.10346	17.414	0.009	0.733 92	Andicam B	Vega
7428.10521	17.378	0.017	0.735 31	Andicam V	Vega
7428.10646	17.250	0.019	0.736 29	Andicam R	Vega
7428.15238	17.202	0.007	0.772 61	OGLE I	Vega
7429.11102	17.266	0.020	0.530 83	Andicam I	Vega
7429.11277	17.449	0.010	0.532 21	Andicam B	Vega
7429.11452	17.458	0.018	0.533 60	Andicam V	Vega
7429.11577	17.358	0.020	0.534 59	Andicam R	Vega
7429.16175	17.156	0.006	0.570 96	OGLE I	Vega
7431.11144	17.391	0.007	0.113 03	OGLE I	Vega
7431.44867	17.194	0.036	0.379 76	UVOT UVW1	AB
7431.51464	17.184	0.034	0.431 94	UVOT UVW1	AB
7431.84659	17.529	0.040	0.694 48	UVOT UVW1	AB
7431.91256	17.453	0.037	0.746 66	UVOT UVW1	AB
7432.12850	17.775	0.010	0.917 46	OGLE I	Vega
7432.37992	17.470	0.036	0.116 32	UVOT UVW1	AB
7432.77229	17.344	0.028	0.426 65	UVOT UVW1	AB
7433.30354	17.717	0.034	0.846 83	UVOT UVW1	AB
7433.83410	17.547	0.058	0.26647	UVOT UVW1	AB
7434.10890	17.560	0.009	0.48382	OGLE I	Vega
7434.37299	17.592	0.034	0.69270	UVOT UVW1	AB
7434.43132	17.762	0.055	0.73883	UVOT UVW1	AB
7435.14184	17.698	0.010	0.30081	OGLE I	Vega
7435.22646	17.722	0.034	0.36774	UVOT UVW1	AB
7435.69174	17.962	0.034	0.73574	UVOT UVW1	AB
7436.29105	18.058	0.034	0.20976	UVOT UVW1	AB
7436.82578	17.938	0.035	0.63269	UVOT UVW1	AB
7437.11450	18.227	0.015	0.86105	OGLE I	Vega
7437.13404	18.188	0.030	0.87650	Andicam I	Vega
7437.13579	18.591	0.042	0.87789	Andicam B	Vega
7437.13759	18.557	0.051	0.87931	Andicam V	Vega
7437.13879	18.450	0.043	0.88026	Andicam R	Vega
7437.74939	17.938	0.040	0.36321	UVOT UVW1	AB
7438.08501	18.074	0.033	0.62866	Andicam I	Vega
7438.08680	18.284	0.036	0.63008	Andicam B	Vega
7438.08855	18.322	0.047	0.63146	Andicam V	Vega
7438.08980	18.169	0.040	0.63245	Andicam R	Vega
7438.28134	18.310	0.054	0.78394	UVOT UVW1	AB
7438.75426	18.231	0.048	0.15799	UVOT UVW1	AB
7439.03049	18.436	0.034	0.37647	Andicam I	Vega
7439.03224	18.409	0.026	0.37785	Andicam B	Vega
7439.03399	18.750	0.054	0.37924	Andicam V	Vega
7439.03524	18.134	0.049	0.38023	Andicam R	Vega
7439.07718	18.113	0.046	0.41340	UVOT UVW1	AB
7439.14844	18.109	0.016	0.46976	OGLE I	Vega
7439.61190	18.517	0.053	0.83633	UVOT UVW1	AB
7440.08900	18.407	0.046	0.21368	Andicam I	Vega
7440.09075	18.555	0.058	0.21507	Andicam B	Vega
7440.09250	18.558	0.063	0.21645	Andicam V	Vega
7440.09375	18.287	0.059	0.21744	Andicam R	Vega
7440.27579	18.234	0.055	0.36142	UVOT UVW1	AB
7440.66955	18.477	0.114	0.67285	UVOT UVW1	AB
7441.02710	18.946	0.048	0.95565	Andicam I	Vega
7441.02885	19.208	0.078	0.95704	Andicam B	Vega

Table A3 – *continued*

Date ^a (MJD)	mag	mag error	Orbital ^c phase	Instrument and filter	phot. system
7441.03064	19.505	0.090	0.95845	Andicam V	Vega
7441.03193	19.299	0.068	0.95948	Andicam R	Vega
7441.10293	18.912	0.035	0.01563	OGLE I	Vega
7441.26816	18.558	0.054	0.14632	UVOT UVW1	AB
7441.73413	18.353	0.051	0.51487	UVOT UVW1	AB
7442.04882	18.085	0.036	0.76377	Andicam I	Vega
7442.05057	18.749	0.051	0.76516	Andicam B	Vega
7442.05236	18.418	0.058	0.76657	Andicam V	Vega
7442.05357	18.637	0.050	0.76753	Andicam R	Vega
7442.39803	18.703	0.060	0.03997	UVOT UVW1	AB
7442.59942	18.553	0.061	0.19925	UVOT UVW1	AB
7443.06192	18.506	0.051	0.56506	UVOT UVW1	AB
7443.09063	18.443	0.025	0.58777	Andicam I	Vega
7443.09354	18.653	0.030	0.59007	Andicam B	Vega
7443.09646	18.646	0.026	0.59238	Andicam V	Vega
7443.09942	18.420	0.024	0.59472	Andicam R	Vega
7443.11736	18.283	0.015	0.60891	OGLE I	Vega
7443.12006	18.260	0.015	0.61105	OGLE I	Vega
7443.65915	18.707	0.052	0.03743	UVOT UVW1	AB
7444.05776	18.544	0.048	0.352 71	UVOT UVW1	AB
7444.65498	18.769	0.058	0.825 07	UVOT UVW1	AB
7445.10716	18.410	0.021	0.182 71	OGLE I	Vega
7445.58555	18.727	0.058	0.561 08	UVOT UVW1	AB
7446.02288	18.822	0.022	0.906 98	Andicam I	Vega
7446.02580	19.104	0.013	0.909 29	Andicam B	Vega
7446.02876	19.037	0.013	0.911 63	Andicam V	Vega
7446.03167	18.932	0.014	0.913 94	Andicam R	Vega
7446.58208	18.709	0.053	0.349 28	UVOT UVW1	AB
7447.04343	18.760	0.021	0.714 18	Andicam I	Vega
7447.04635	19.181	0.013	0.716 49	Andicam B	Vega
7447.04931	18.919	0.012	0.718 83	Andicam V	Vega
7447.05226	18.733	0.013	0.721 16	Andicam R	Vega
7447.13940	18.686	0.018	0.790 08	OGLE I	Vega
7448.02695	18.666	0.020	0.492 07	Andicam I	Vega
7448.02987	19.180	0.012	0.494 38	Andicam B	Vega
7448.03278	18.816	0.012	0.496 68	Andicam V	Vega
7448.03574	18.747	0.013	0.499 02	Andicam R	Vega
7448.57723	18.717	0.063	0.927 31	UVOT UVW1	AB
7449.01826	18.687	0.026	0.276 13	Andicam I	Vega
7449.02118	19.233	0.014	0.278 44	Andicam B	Vega
7449.02413	18.792	0.014	0.280 77	Andicam V	Vega
7449.02705	18.831	0.016	0.283 08	Andicam R	Vega
7449.10640	18.584	0.049	0.345 85	UVOT UVW1	AB
7449.12580	18.459	0.022	0.361 19	OGLE I	Vega
7449.57168	18.710	0.054	0.713 85	UVOT UVW1	AB
7450.01960	18.771	0.023	0.068 13	Andicam I	Vega
7450.02252	19.008	0.012	0.070 44	Andicam B	Vega
7450.02547	18.906	0.013	0.072 77	Andicam V	Vega
7450.02839	18.871	0.015	0.075 08	Andicam R	Vega
7450.03835	18.803	0.062	0.082 96	UVOT UVW1	AB
7450.56752	18.696	0.053	0.501 50	UVOT UVW1	AB
7451.10166	18.873	0.023	0.923 96	Andicam I	Vega
7451.10462	19.208	0.014	0.926 30	Andicam B	Vega
7451.10758	19.187	0.013	0.928 65	Andicam V	Vega
7451.11049	19.006	0.014	0.930 95	Andicam R	Vega
7451.16683	19.312	0.076	0.975 51	UVOT UVW1	AB
7452.02922	18.656	0.024	0.657 60	Andicam I	Vega
7452.03213	18.898	0.012	0.659 90	Andicam B	Vega
7452.03509	18.904	0.012	0.662 24	Andicam V	Vega
7452.03801	18.889	0.015	0.664 55	Andicam R	Vega
7453.04974	18.816	0.021	0.464 76	Andicam I	Vega
7453.05269	19.243	0.013	0.467 09	Andicam B	Vega
7453.05561	18.963	0.013	0.469 40	Andicam V	Vega

Table A3 – continued

Date ^a (MJD)	mag	mag error	Orbital ^c phase	Instrument and filter	phot. system
7453.05853	18.963	0.015	0.471 71	Andicam R	Vega
7453.10025	18.718	0.019	0.504 71	OGLE I	Vega
7453.49185	19.068	0.110	0.814 44	UVOT UVM2	AB
7453.49532	18.899	0.109	0.817 19	UVOT UVW1	AB
7453.49671	18.253	0.104	0.818 29	UVOT U	AB
7453.49810	19.300	0.086	0.819 39	UVOT UVW2	AB
7454.03666	19.264	0.088	0.245 35	Andicam B	Vega
7454.03958	19.125	0.079	0.247 66	Andicam V	Vega
7454.04249	18.981	0.029	0.249 97	Andicam R	Vega
7455.88284	18.955	0.156	0.705 56	UVOT UVM2	AB
7455.88423	18.822	0.160	0.706 66	UVOT UVW1	AB
7455.88492	18.074	0.153	0.707 21	UVOT U	AB
7455.88562	19.110	0.112	0.707 75	UVOT UVW2	AB
7455.94881	18.834	0.098	0.757 74	UVOT UVM2	AB
7455.95159	18.715	0.100	0.759 93	UVOT UVW1	AB
7455.95367	18.417	0.122	0.761 58	UVOT U	AB
7455.95506	19.098	0.076	0.762 68	UVOT UVW2	AB
7456.01465	18.848	0.025	0.809 81	Andicam I	Vega
7456.01757	19.081	0.014	0.812 12	Andicam B	Vega
7456.02053	19.213	0.015	0.814 46	Andicam V	Vega
7456.02348	18.934	0.016	0.816 79	Andicam R	Vega
7457.01450	18.757	0.023	0.600 62	Andicam I	Vega
7457.01746	19.018	0.013	0.602 96	Andicam B	Vega
7457.02042	18.965	0.013	0.605 30	Andicam V	Vega
7457.02338	18.739	0.013	0.607 65	Andicam R	Vega
7457.11303	18.722	0.022	0.678 56	OGLE I	Vega
7457.41619	18.944	0.089	0.918 33	UVOT UVM2	AB
7457.42035	18.860	0.089	0.921 63	UVOT UVW1	AB
7457.42313	18.644	0.103	0.923 82	UVOT U	AB
7457.42452	19.066	0.063	0.924 92	UVOT UVW2	AB

^aThe full set of collected photometric and spectroscopic data on N LMC 1968 will be submitted to the IAU astronomical data centres.

^bTime of exposure; mid-time if possible.

^cFrom equation (2).

¹Mullard Space Science Laboratory, University College London, Holmbury St. Mary, Dorking, Surrey RH5 6NT, UK

²X-Ray and Observational Astronomy Group, School of Physics & Astronomy, University of Leicester, Leicester LE1 7RH, UK

³Astronomical Observatory, University of Warsaw, Al. Ujazdowskie 4, PL-00-478 Warszawa, Poland

⁴Astrophysics Research Institute, Liverpool John Moores University, IC2, Liverpool Science Park, Liverpool L3 5RF, UK

⁵Dipartimento di Fisica ‘Enrico Fermi’, Università di Pisa, I-56127 Pisa, Italy

⁶NFN-Sezione Pisa, largo B. Pontecorvo 3, I-56127 Pisa, Italy

⁷Department of Physics and Astronomy, Stony Brook University, Stony Brook, NY 11794-3800, USA

⁸Las Campanas Observatory, Carnegie Observatories, Casilla 601, La Serena, Chile

⁹INAF-Astronomical Observatory of Padova, I-36012 Asiago (VI), Italy

¹⁰Mirranook Observatory, Boorolong Rd, Armidale, NSW 2350, Australia

¹¹Astrophysics Group, Keele University, Keele, Staffordshire ST5 5BG, UK

¹²Minnesota Institute for Astrophysics, School of Physics & Astronomy, University of Minnesota, Minneapolis, MN 55455, USA

¹³School of Earth and Space Exploration, Arizona State University, Box 871404, Tempe, AZ 85287-1404, USA

¹⁴Institut de Ciències de l’Espai (CSIC-IEEC), Campus UAB, C/Can Magrans s/n, E-08193 Cerdanyola del Valles, Spain

¹⁵Department of Astronomy, San Diego State University, San Diego, CA 92182, USA

¹⁶Physics Department, Lancaster University, Lancaster LA1 4YB, UK

¹⁷American Astronomical Society, 2000 Florida Ave., NW, Suite 400, DC 20009-1231, USA

¹⁸Department of Astronomy, Ohio State University, 140 W 18th Ave., Columbus, OH 43210, USA

¹⁹CIDMA, Departamento de Física, Universidade de Aveiro, Campus Universitário de Santiago, P-3810-193 Aveiro, Portugal

²⁰Instituto de Telecomunicações, Campus Universitário de Santiago, P-3810-193 Aveiro, Portugal

²¹Instituto de Investigación Multidisciplinar en Ciencia y Tecnología, Universidad de La Serena, Av. R. Bitrán 1305, La Serena, Chile

²²Departamento de Física y Astronomía, Universidad de La Serena, Av. J. Cisternas 1200, 172-0236 La Serena, Chile

This paper has been typeset from a $\text{\TeX}/\text{\LaTeX}$ file prepared by the author.